

Key Points:

- The global abundance of plagioclase, pyroxene and olivine are presented
- The effects of space weathering on Christiansen Feature maps are removed with an improved algorithm
- New silica-rich locations are identified in the Oceanus Procellarum region

Correspondence to:




P. G. Lucey,
lucey@higp.hawaii.edu

Citation:

Lucey, P. G., Greenhagen, B., Hanna, K. D., Bowles, N., Flom, A., & Paige, D. A. (2021). Christiansen feature map from the lunar reconnaissance orbiter diviner lunar radiometer experiment: Improved corrections and derived mineralogy. *Journal of Geophysical Research: Planets*, 126, e2020JE006777. <https://doi.org/10.1029/2020JE006777>

Received 18 NOV 2020
 Accepted 12 APR 2021

Christiansen Feature Map From the Lunar Reconnaissance Orbiter Diviner Lunar Radiometer Experiment: Improved Corrections and Derived Mineralogy

Paul G. Lucey¹ , Benjamin Greenhagen², Kerri Donaldson Hanna³ , Neil Bowles⁴, Abigail Flom¹ , and David A. Paige⁵

¹Hawaii Institute of Geophysics and Planetology, University of Hawaii at Manoa, Honolulu, HI, USA, ²The Johns Hopkins University Applied Physics Laboratory, Laurel, MD, USA, ³University of Central Florida, Orlando, FL, USA, ⁴Atmospheric, Oceanic and Planetary Physics, Clarendon Laboratory, Oxford University, Oxford, UK, ⁵University of California at Los Angeles, Los Angeles, CA, USA

Abstract Maps of plagioclase, olivine, and pyroxene at 1 km resolution are derived from a combination of data from the Diviner Lunar Radiometer on the Lunar Reconnaissance Orbiter and the Kaguya Multiband Imager. The Diviner instrument features three infrared bands designed to characterize a spectral feature of lunar soils that is sensitive to the average silica polymerization of the surface called the Christiansen Feature, which is directly sensitive to the presence of plagioclase, the dominant lunar silicate. Existing global mineral maps based on near-IR data largely infer the presence of plagioclase from the bright mineral's effect on total reflectance, excepting in rare locations where the surface is nearly pure plagioclase and a weak feature in the plagioclase near-IR spectrum can be relied upon. By integrating both wavelength regions we produced more robust estimates of the abundance of the three dominant minerals. In the process of this work, we also improved the removal of space weathering effects from Christiansen Feature maps, and showed that silica rich compositional anomalies could be reliably detected by decorrelating Christiansen Feature and FeO maps. New silica-rich locations are reported as are the global abundances of the three major silicates.

Plain Language Summary One of the goals of remote sensing of the Moon is to produce maps of the minerals present on its surface. In this paper, we bring together two infrared spectroscopic data sets to create maps of the minerals plagioclase, pyroxene, and olivine at a resolution of 1 km. One of these infrared data sets defines the wavelength position of a spectral phenomenon called the Christiansen Feature that is sensitive to the presence of unusual silica-rich minerals that indicate a relatively rare but widespread style of lunar volcanism. Using these new data, we find a few previously unrecognized silica-rich exposures that extend the spatial range of these features. The Christiansen Feature is also sensitive to rare rock types that may represent outcrops of the lunar mantle at the surface of the Moon, and a promising candidate is revealed at the farside crater Titov.

1. Introduction

The major mineralogy of the Moon is relatively simple, with the vast majority of the lunar crust being composed of four minerals: plagioclase, pyroxene, olivine, and ilmenite (and the latter is a major constituent only in a few restricted areas in the lunar maria). In the anorthositic lunar highlands the surface is largely a mixture of plagioclase and low calcium pyroxene, while in the basaltic maria the surface is a more mafic assemblage with a diverse assemblage of pyroxenes (e.g., Moriarty III, D. P., & Pieters, C. M., 2016).

Solutions to key questions about the development of the lunar crust rely on quantitative understanding of these mixtures. Does the crust become more mafic with depth? That is does is an hypothesis developed from the characteristics of basaltic impact melts of basin origin (Ryder & Wood, 1977), and the question hinges on the relative abundance of plagioclase and pyroxene in central peaks of large craters across the Moon that can be used to probe the composition of the crust with depth (Cahill et al., 2009; Cahill & Lucey, 2007; Lemelin et al., 2015; Martinot et al., 2018; Moriarty, Pieters, & Isaacson, 2013; Nakamura et al., 2009; Runyon

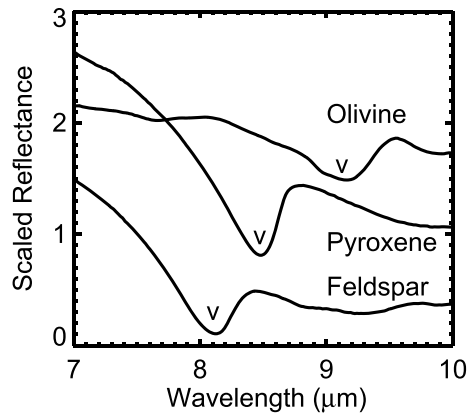


Figure 1. Reflectance spectra of the feldspar anorthite, the pyroxene augite, and an olivine of composition Fo50. The small arrows indicate the position of the Christiansen Feature minimum in these spectra. In emission, the feature is a peak.

et al., 2020; Song et al., 2013; Tompkins & Pieters, 1999). Are outcrops of the lunar mantle present in the rings of large impact basins or in central peaks of large craters? This question hinges on the relative abundance of plagioclase and mafic minerals in anomalies like the central peak of the lunar crater Copernicus and the rings of impact basins (Arnold et al., 2016; Bretzfelder et al., 2020; Lucey et al., 2014; Melosh et al., 2017; Moriarty et al., 2020; Pieters & Wilhelms, 1985; Yamamoto et al., 2010).

Global maps of mineral concentrations have been developed from near-IR data to address these very questions (e.g., Lemelin et al., 2019). However, near-IR spectral reflectance is an imperfect tool for understanding the relative abundance of plagioclase and mafic minerals. While plagioclase can exhibit a diagnostic absorption feature in its spectrum at 1,250 nm due to trace amounts of iron within its crystal structure, this feature is susceptible to shock (Bruckenthal & Pieters, 1984) and masking by space weathering (Lucey, 2002) and to variations in the abundance of the iron impurity in the feldspar (Cheek & Pieters, 2014). The primary indicator of plagioclase exploited by mineral mapping algorithms using near-IR data is the fact that plagioclase is high in albedo compared to its mafic counterparts. In other words, mapping of plagioclase largely relies upon

the lack of absorption, rather than keying on a diagnostic spectral feature of the mineral. This reliance has been successful, as estimates of uncertainty in extraction of mineral abundances has been shown to have about 10% accuracy (Cahill & Lucey, 2007; Lemelin et al., 2015), but the reliance on the lack of absorption requires excellent and confident mitigation of other factors that might affect the brightness of a surface, including the particle size of the surface and the degree to which space weathering has altered the reflectance.

In contrast, a thermal infrared spectral feature directly sensitive to plagioclase has been well-characterized by the Diviner Lunar Radiometer in a decade of operation on the Lunar Reconnaissance Orbiter. Silicates are very strongly absorbing near $9 \mu\text{m}$, a phenomenon governed by the imaginary index of refraction of the mineral in this region. At wavelengths slightly shorter than those of strong absorption, the real index of refraction undergoes rapid variation, and in the thermal infrared goes through a value of one, where it matches the index of the surrounding medium (i.e., air or vacuum). This passage of the real index through that of the medium is called the Christiansen Frequency. This phenomenon gives rise to a strong minimum in reflectance and a maximum in emission in spectra of particulate silicate samples (Conel, 1969). Where the index matches that of air or vacuum, scattering is minimized so photons can travel farther in a sample in reflectance and have a greater probability of absorption giving rise to a reflectance minimum. In emission, photons originating as blackbody radiation within the surface have a higher probability of escaping the surface at that wavelength, and so the phenomenon results in an emission maximum. Because of the influence of scattering, thermal gradients and mixtures, the Christiansen Frequency and Christiansen Feature are not precisely at the same positions, hence the distinction in nomenclature between a precise physical phenomenon in the optical constants of particular materials (the Christiansen Frequency) and its manifestation in the spectrum of a particulate (the Christiansen Feature). However, they are closely related and the position of the Christiansen Feature is largely due to the position of the Christiansen Frequency. Hereafter, when we use the acronym “CF,” it refers to the Christiansen Feature as observed in emission or reflectance spectra.

The Christiansen Feature is important in lunar remote sensing because the spectral contrast of vibrational features are somewhat suppressed by the fine grain sizes characteristic of lunar soil (Lyon, 1965), but the Christiansen Feature and its wavelength sensitivity to composition persists. Of the three major lunar minerals, the framework silicate anorthite feldspar has the highest bond energy and the shortest of the Christiansen Feature positions. The vast majority of lunar feldspar is Ca-rich plagioclase (anorthite), and its Christiansen Feature position measured in reflectance is near $7.9 \mu\text{m}$ (Salisbury et al., 1991, Figure 1). The chain silicate pyroxene is next in bond strength and in the wavelength position of the Christiansen Feature. Pyroxenes show little variation in Christiansen Feature position with chemistry, with the reflectance minimum near $8.2 \mu\text{m}$ (Salisbury et al., 1991). Finally, olivine, with its isolated silicate tetrahedra, has its Christiansen Feature wavelength at the lowest frequency. The wavelength position is strongly dependent on

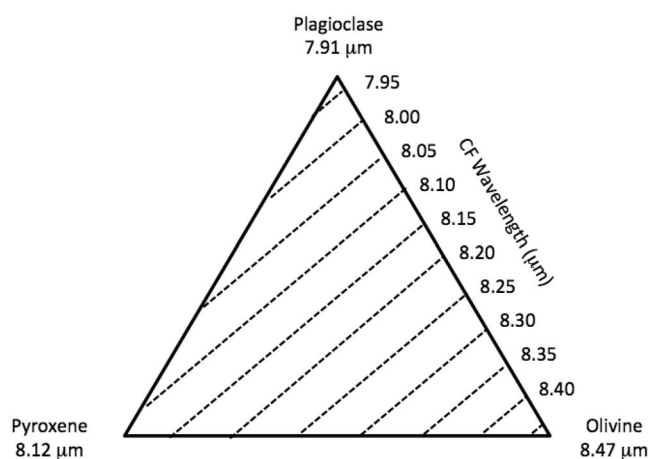


Figure 2. Illustration of the effect of composition on the position of the Christiansen Feature. On this ternary diagram of plagioclase, pyroxene and olivine, a particular Christiansen Feature wavelength can arise from a series of mixtures that cut across the ternary.

olivine chemistry, with the magnesium endmember forsterite exhibiting in reflectance a minimum at 8.5 μm and the iron endmember fayalite at 9.4 μm (Salisbury et al., 1991).

The CF positions of particulate silicates measured in reflectance hold for emission spectra as well, provided the samples are isothermal. Particulate samples are isothermal under ambient pressure conditions in terrestrial laboratories where gas conduction equalizes temperatures. Under this condition hemispherical reflectance and emission spectra are related by Kirchhoff's Law and sum to unity if transmission is assumed to be zero ($\epsilon = 1 - R - T$). However, in the case of emission on the Moon, spectral contrast is amplified by the presence of strong thermal gradients in the uppermost surface. Near the Christiansen Frequency position the spectrum probes more deeply into the surface where temperatures are higher, causing a more prominent emission peak than is present in an isothermal surface (Donaldson Hanna et al., 2017; Henderson & Jakosky, 1994; Logan et al., 1973). Thermal gradients are due in part due to the difference between optical transparency at visible wavelengths where solar radiation is deposited, and the infrared wavelengths where the thermal radiation is emitted. In the visible, lunar soils are relatively transparent, so solar energy is deposited over a few grain diameters. In contrast, at most thermal

wavelengths grains are essentially opaque, so radiative cooling occurs only at the immediate surface. This allows a thermal gradient to develop, where there is a steep rise in temperature over the scale of a few grains. There is some variation in infrared opacity with wavelength, so infrared emission probes the thermal gradient with wavelength, analogous to probing temperature in infrared spectra of planetary atmospheres. The resultant spectrum is a combination of the inherent spectral emissivity variations of the surface, and the variations in probe depth (Henderson & Jakosky, 1994). A consequence of this is that the CF position shifts to shorter wavelength with the intensity of the thermal gradient.

The CF, being a single parameter, cannot uniquely determine the relative abundances of the lunar silicates. The CF position of a portion of the lunar surface is combination of those all of the silicates present, weighted by their abundances. For example, if a surface exhibited a CF position the same as that of pyroxene, because the CF positions of plagioclase and olivine bracket that of pyroxene, the measured CF could represent a pure pyroxene, a two-component mixture of olivine and plagioclase, or a series of mixtures of all three. Thus, a given CF position defines a locus that cuts across the ternary diagram of plagioclase, pyroxene, and olivine (Figure 2). (Oxides are spectrally flat in the region of the silicate CF, and exhibit a shallow, broad emission maximum around 10–15 μm).

This issue can be mitigated by combining the CF position with independent information on mafic mineralogy using near-IR data. Arnold et al. (2016) exploited this in a study of olivine-rich regions that were suspected to be exposures of lunar mantle material that would be indicated by the presence of dunite (Yamamoto et al., 2010), an ultramafic rock composed of more than 90 percent olivine. NIR spectra of the candidate locations showed them to be essentially free of pyroxene owing to high sensitivity of near-IR spectroscopy to that mineral (Yamamoto et al., 2010), but the relative abundance of plagioclase and olivine was highly uncertain due both to the indirect nature of plagioclase detection, the nonlinearity of mixing at NIR wavelengths, and the spectral similarity between olivine and plagioclase that makes determining mineral ratios of that pair uncertain (Cheek & Pieters, 2014). Because Arnold et al., (2016) could exclude pyroxene in their analysis, they could confidently infer the plagioclase-olivine ratio and conclude that the CF position of the mantle candidates were too short to represent nearly pure olivine; the mantle candidates were thus shown to be composed of troctolite, a rock type plausibly attributed to crustal igneous processes, and not the ultramafic rock suspected to represent mantle (though we note that at higher spatial resolution the average composition of troctolite could resolve into spatially distinct patches of anorthosite and dunite).

In this study, we extend the pioneering work of Arnold et al. (2016) by incorporating in our CF analysis ratios of olivine and pyroxene derived from radiative transfer models of near-IR data to arrive at unique solutions for plagioclase content Moonwide. Mineral abundances of olivine and pyroxene are obtained

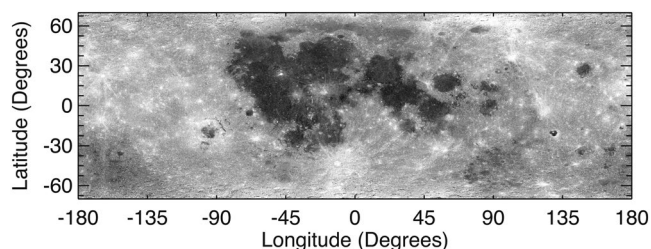


Figure 3. Image of the Christiansen Feature from the Diviner Lunar Radiometer Experiment. Data are plotted as the inverse of wavelength, with $8\ \mu\text{m}$ as black and $8.4\ \mu\text{m}$ as white. Note the prominent ray patterns associated with Copernican craters such as Tycho (lower center). Projection is simple cylindrical, longitude covers $\pm 180^\circ$, latitude is $\pm 70^\circ$.

by combining the CF with estimates of olivine to pyroxene ratio using near-IR iron absorptions, thus our algorithm exploits spectral features for all minerals that are directly sensitive to their presence. Combining this independent estimate for plagioclase content with the previously established ratio of pyroxene and olivine provides a new estimate of abundances for all these silicates.

Before derivation of mineralogy from the CF, we must accommodate the fact that the CF position is affected by space weathering of the lunar surface, a result not anticipated prior to the LRO mission. Thermal IR reflectance spectroscopy of lunar soils showed no measurable effect of space weathering on the Christiansen Feature position (Salisbury et al., 1997). Additionally, analog plagioclase samples vitrified to capture the effect of abundant lunar glass that accumulates with exposure to space showed no shifts in wavelength position with glass content (Nash & Salisbury, 1991).

So it came as a surprise when maps of the Diviner CF value were first produced, and young fresh craters showed vivid low-CF ejecta and ray patterns that closely matched their distribution in the visible portion of the spectrum (Greenhagen et al., 2010). Indeed, global mosaics of CF value depicted in grayscale are difficult to distinguish from visible images of the Moon. Lucey et al. (2017) investigated this new finding and concluded that the space weathering effect was likely due to the influence of albedo on the thermal gradients within the lunar optical surface, but that the compositional influence on CF position was still present, showing that high-silica and high olivine locations with their highly anomalous CF values fell strongly off the albedo-CF value trend. They also developed a correction for space weathering using an optical maturity parameter derived from visible and near-IR images of the Moon. That treatment was reasonably successful at removing space weathering effects, but had *ad hoc* aspects that will be improved upon here.

In this study, we will present:

1. The improved space weathering correction to the CF data
2. The algorithm for derivation of plagioclase from the CF supported by Kaguya olivine/pyroxene ratios
3. The abundance of plagioclase and the mafic minerals
4. The results of decorrelating the CF and prior FeO estimates to produce a new parameter sensitive to the presence of silica and ultramafic anomalies.

2. Data and Methods

Here we use Diviner's three narrow-band channels near $8\ \mu\text{m}$ to estimate the wavelength of the CF position. We retrieved PDS-archived calibrated radiances collected by Diviner between July 2009 and May 2016. For each orbit, data between 70S and 70N were projected on a topographic grid using the method of Williams et al. (2016) and binned into 32 pixel per degree cylindrical bins. We then followed the method of Greenhagen et al., 2010 to first calculate emissivity and use a parabolic fit to estimate the CF value within each bin. Diviner-derived CF values deviate systematically from the CF position determined from high-resolution spectra, and these deviations are well-understood (Greenhagen et al., 2010, SOM). Previous studies have noted the dependences of CF value on illumination and topography (e.g., Greenhagen et al., 2010; Lucey et al., 2017). Therefore, our data were "photometrically" corrected by projecting the data onto a high-resolution topographic grid, calculating photometric geometry, and applying the empirical correction methodology "CX3" (Greenhagen et al., 2010, 2011). While this correction improved the topographic influence, at higher latitudes (approximately above 50°) the presence of macroscopic shadows allows some artifacts to remain. Finally, to minimize data outliers, the median of all CF values (one for each orbit present in a given 32 ppd bin) were tabulated to produce the global CX3 CF value map (Figure 3) with a wavelength certainty of $0.02\ \mu\text{m}$

The mineral abundances of plagioclase, olivine, low-Ca pyroxene and high-Ca pyroxene as well as FeO and OMAT were derived from SELENE Multi-band Imager (MI) multispectral imaging with a radiative transfer model by Lemelin et al. (2015). The mineral maps contain striping at the 5 wt. % level due to uncertainties

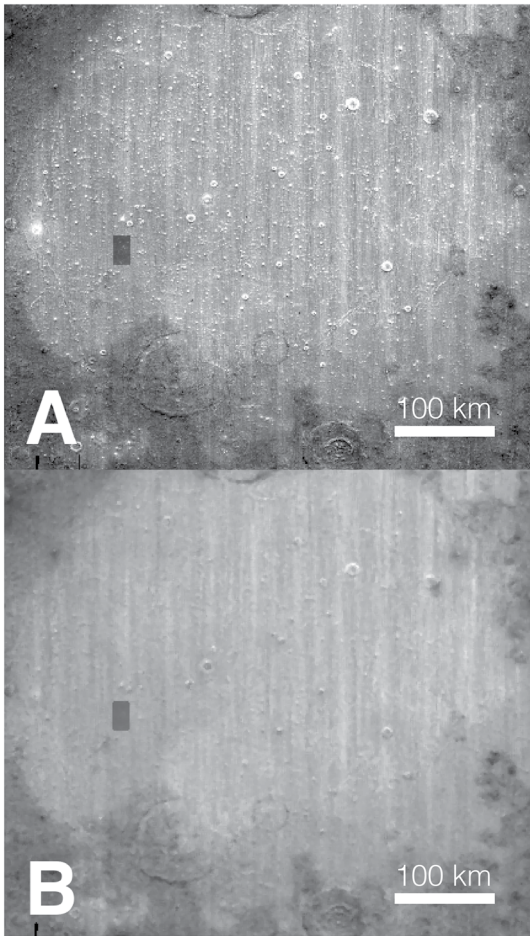


Figure 4. Corrected CF images of Mare Humorum. (a) Image corrected with Lucey et al. (2017) space weathering compensation algorithm showing substantial overcorrection of immature craters in the maria. (b) Image corrected using the new algorithm described in the text. CF, Christiansen Feature

in photometric correction of the underlying MI data, and the best data quality can be found at latitudes below 60° north and south, and are the focus of the analysis in this paper.

2.1. Space Weathering: Improved Mitigation

Space weathering strongly influences the wavelength position of the lunar Christiansen Feature. Figure 3 shows the global CX3 CF value map in simple cylindrical projection, plotted so that low CF values are bright and high CF values are dark to illustrate the presence of anomalies associated with fresh craters. Lucey et al. (2017) showed that crater rays and steep slopes with high albedo at visible wavelengths are also anomalous in CF value. They presented a correction for this effect using the optical maturity parameter OMAT (Lucey et al., 2000) derived from Kaguya Multiband Imager near-IR data that largely removed the anomalies in highland terrain. After the application of their correction, the space weathering anomalies were strongly reduced. However, the correction was only partly successful in the maria, and application still left significant anomalies with strong variations associated with space weathering such as in the vicinity of small fresh craters. Figure 4 shows a portion of Mare Humorum before and after the Lucey et al. (2017) correction. The space weathering correction optimized for highland values has substantially overcorrected the space weathering effects in the maria, meaning that the contrast associated with OMAT in iron rich terrains is too great. We found through experimentation that properly scaling OMAT could produce a quality correction in the maria or the highlands, but no single scale factor would produce an effective correction for both maria and highlands. The optimum scale factor for the highlands correction is close to unity. However in the maria, the contrast in OMAT associated with variations in space weathering (relative values from mature to immature features) is about a factor of 2 too high compared to the observed contrast in CF data for the maria. We reasoned that because the mare and highlands differ principally in iron content, we could develop a correction proportional to iron. This was effective. A flow chart outlining the correction is shown in Figure 5.

Our improved correction has these constraints. First, as the existing correction is effective in highland terrain the improved correction should have little change when applied on low iron highlands. Second, because by its nature OMAT has little sensitivity to composition in mature terrains, the correction should not create any difference between highland and maria in mature terrains. In brief, the correction should reduce the OMAT value of immature surfaces in high iron mare terrains by about a factor of two, but otherwise leave values largely unchanged. To prevent much change in mature areas, the mode of the Kaguya Multiband Imager OMAT histogram is subtracted from the Kaguya Multiband Imager OMAT parameter (Lemelin et al., 2015). Because the vast majority of the lunar surface is mature, this subtraction places most mature surfaces near zero, so those values will be largely unchanged when a multiplicative FeO parameter is applied.

$$\text{OMAT}_{\text{scaled}} = \frac{\text{OMAT} - \text{OMAT}_{\text{mode}}}{\text{FeO}_{\text{parameter}}} \quad (1)$$

In its design, the FeO parameter itself should have little to no effect in iron poor terrains as the original correction works well in the highlands. The FeO parameter itself uses the FeO wt. % data set of Lemelin et al. (2015) (see Section 2). We then subtract from this data set its mode (in units of weight percent) so that the iron poor highlands that dominated the mode have a mean near zero. We then apply a scale factor (with

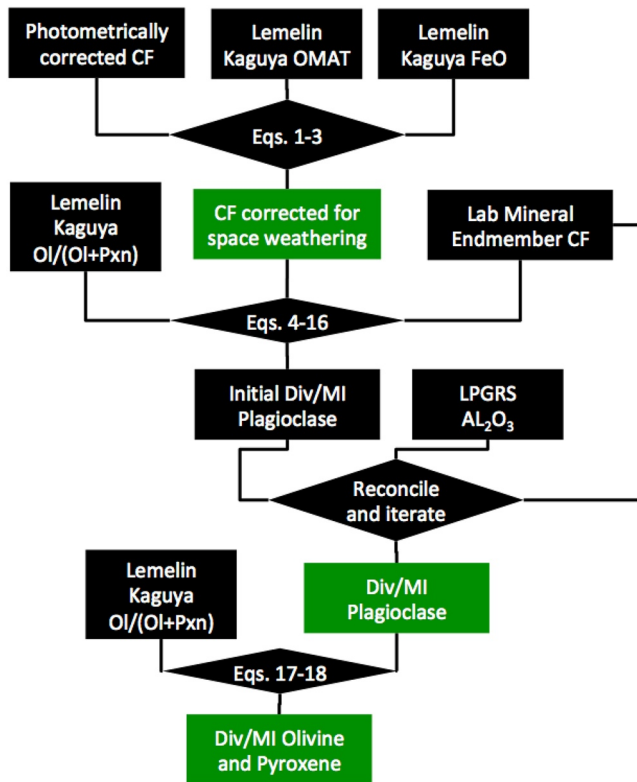


Figure 5. Flowchart showing the processing done in this study. Green boxes are outputs, black are inputs or operations.

2.2. Mineral Algorithm

The Christiansen Feature position, being a single parameter, cannot be used on its own to define lunar mineralogy which to a large degree is a mixture of the three components, plagioclase, pyroxene, and olivine (Figure 9). The Christiansen Feature position of a lunar soil, a mixture of those minerals, will exhibit a relative value that reflects the CF positions of its constituent endmembers. The principal issue is that with pyroxene having a CF value intermediate to those of olivine and feldspar, there is ambiguity between various mixtures that all can share the same CF values. This is illustrated in Figure 10 that treats the CF position of a mixture as a linear combination of the CF values of its endmembers. On that ternary diagram, loci of constant CF cross a wide range of compositions. For example, basalts are mixtures of approximately equal abundances of plagioclase and pyroxene; the CF of a troctolite (plagioclase-olivine mixture) could share the same CF position as the basalt.

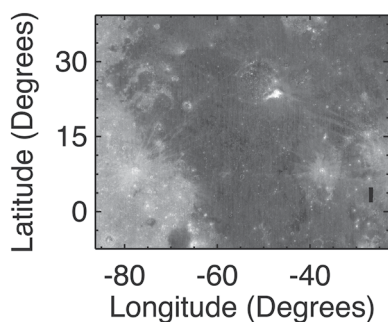


Figure 6. CF image plotted as inverse from 8.4 to 8 μm . Space weathering effects are evident in fresh craters both in the maria and the highland, where bright spots are fresh impact craters. CF, Christiansen Feature

value determined below) to the zero-meaned FeO data, then add 1. The result is an FeO sensitive correction parameter that has values near unity in highland terrain, but values larger than one in mare terrain.

$$\text{FeO}_{\text{parameter}} = \frac{\text{FeO} - \text{FeO}_{\text{mode}}}{\text{FeO}_{\text{scale}} + 1}, \quad (2)$$

where FeO and FeO_{mode} are in units of weight percent, and $\text{FeO}_{\text{scale}}$ is unitless. The net result of Equations 1 and 2 is an adjusted OMAT parameter that has values near zero for mature surfaces in the mare and highland. The original, effective, OMAT values for immature surfaces in the highlands are preserved (less the mode of the original OMAT), and values in immature maria are reduced relative to the original OMAT values.

This parameter is applied per Lucey et al. (2017):

$$\text{CF}_{\text{corrected}} = \text{CF} + \text{OMAT}_{\text{scaled}}. \quad (3)$$

The net result is that the corrected CF in mature terrains is little changed from the input CF; immature surfaces are altered relative to their FeO difference between the modal FeO value and their local iron content.

The parameter $\text{FeO}_{\text{scale}}$ in Equation 2 is determined empirically by examining the quality of the space weathering correction in test regions of maria. We adjusted the value of $\text{FeO}_{\text{scale}}$ while monitoring several mare surfaces at full resolution and found that a value of 15 minimized the difference between the apparent CF of small fresh craters and their ejecta, and the mature mare background. Figure 4 shows the improved result of the correction in Mare Humorum, while Figures 6 and 7 show the results in the large Oceanus Procellarum region. The new algorithm substantially reduces the sensitivity of the final data set to space weathering effects in the maria, while preserving good performance in the highlands. Figure 8 shows the global result of the new correction.

To resolve this ambiguity we turn to near-IR spectroscopy. At near infrared wavelengths the iron-bearing minerals olivine and pyroxene exhibit diagnostic spectral characteristics that are highly distinct from one another. Mineral abundance maps have been produced using data from Clementine (Lucey, 2004), and from the Kaguya Multiband Imager (Lemelin et al., 2015), based on spectral mixing models

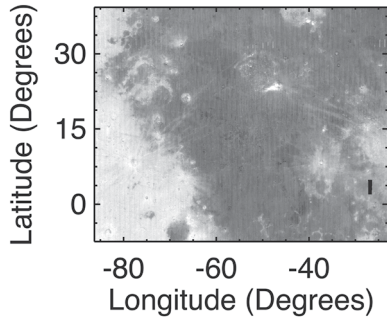


Figure 7. CF image corrected for space weathering using the algorithm described in the text, plotted as inverse from 8.4 to 8. Space weathering effects are largely subdued in both highland and mare terrains. CF, Christiansen Feature.

that exploit the strong spectral differences between these minerals. These maps also include estimates of feldspar abundance, and the presence of feldspar is inferred from a weak absorption feature near 1,250 nm and from the indirect influence of feldspar on the albedo of the surface.

We exploit this strength to resolve the Diviner CF ambiguity. On the ternary diagram shown in Figure 11 lines of constant olivine-pyroxene ratio are nearly orthogonal to the loci of constant CF; and given both, a lunar composition can be uniquely determined.

To compute composition from CF and the NIR-derived mafic ratio, we place the compositional ternary diagram in a Cartesian framework with the pyroxene endmember corner at the origin, and define the equilateral triangle as having height 1.0 (Figure 12). This gives sides of length $2/\sqrt{3}$. In this framework, the CF and NIR loci define lines and we solve simultaneously for the solution. In terms of actual CF and NIR ratios, the coordinates of the intercepts with the triangle by the NIR locus are:

$$X_{\text{NIR}} = \frac{\text{OL (wt.\%)}}{\text{OL (wt.\%) + Pyroxene (wt.\%)} * \frac{2}{\sqrt{3}}}, \quad (4)$$

$$Y_{\text{NIR}} = 0, \quad (5)$$

$$X_{2\text{NIR}} = \frac{1}{\sqrt{3}}, \quad (6)$$

$$Y_{2\text{NIR}} = 1, \quad (7)$$

where the NIR line is defined by the plagioclase vertex and the ol/ol + px ratio of the pixel in question along the base of the triangle.

For the intercept points of the CF line:

$$X_{1\text{CF}} = \frac{\tan(30) [\text{CF}_{\text{pxn}} - \text{CF}_x]}{\text{CF}_{\text{pxn}} - \text{CF}_{\text{plg}}}, \quad (8)$$

$$Y_{1\text{CF}} = \frac{\text{CF}_{\text{pxn}} - \text{CF}_x}{\text{CF}_{\text{pxn}} - \text{CF}_{\text{plg}}}, \quad (9)$$

$$X_{2\text{CF}} = \frac{2}{\sqrt{3}} - \frac{\tan(30) [\text{CF}_{\text{ol}} - \text{CF}_x]}{\text{CF}_{\text{ol}} - \text{CF}_{\text{plg}}}, \quad (10)$$

$$Y_{2\text{CF}} = \frac{\text{CF}_{\text{ol}} - \text{CF}_x}{\text{CF}_{\text{ol}} - \text{CF}_{\text{plg}}}, \quad (11)$$

where CF_x is the CF of the pixel under consideration, and CF_{plg} , CF_{pxn} , and CF_{ol} are the CF's assigned to the endmembers.

After some tedious algebra:

$$\text{Plagioclase (wt.\%)} = \frac{m_{\text{CF}} (b_{\text{CF}} - b_{\text{NIR}})}{m_{\text{NIR}} - m_{\text{CF}}} + b_{\text{CF}}, \quad (12)$$

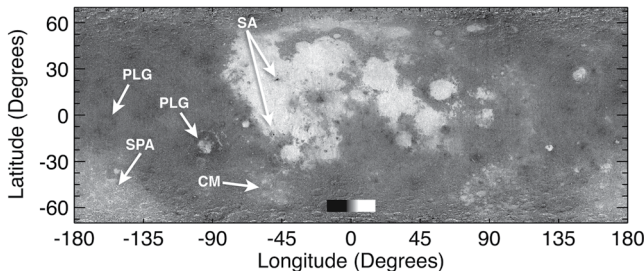


Figure 8. Global CF data corrected for space weathering. Image stretch from 8 to 8.4 μm .

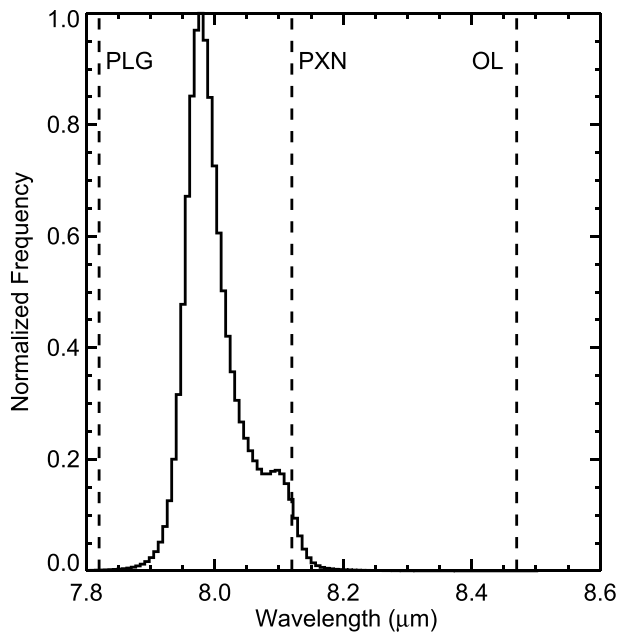


Figure 9. Histogram of space weathering corrected CF, with CF positions of plagioclase, pyroxene, and olivine shown. This illustrates that lunar CF values can be derived from mixtures of plagioclase with either mafic mineral, or plagioclase with some combination of mafic minerals. Endmember positions from Donaldson Hanna et al. (2012a, 2012b). CF, Christiansen Feature.

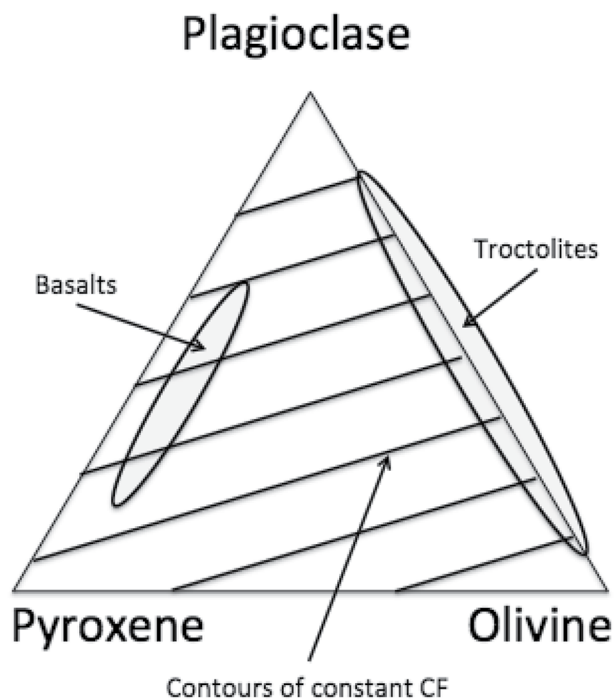


Figure 10. Cartoon of CF compositional ambiguity effect. The inclined lines are constant CF values that cut across the lunar silicate mineral ternary diagram. Basalts can share the same CF value with troctolites, despite their critically different implications for lunar crustal evolution. CF, Christiansen Feature.

where:

$$m_{CF} = \frac{Y_{2CF} - Y_{1CF}}{(2 / \sqrt{3}) \tan(30) Y_{2CF}} - \tan(30) Y_{1CF}, \quad (13)$$

$$b_{CF} = -m_{CF} (\tan(30) Y_{1CF}) + Y_{1CF}, \quad (14)$$

$$m_{NIR} = \frac{1}{(1 / \sqrt{3}) - 2 OL (wt.%) / \sqrt{3} * (OL (wt.%) + Pyroxene (wt.%))}, \quad (15)$$

$$b_{NIR} = -m_{NIR} \frac{(2 / \sqrt{3}) OL (wt.%) }{OL (wt.%) + Pyroxene (wt.%)}. \quad (16)$$

The m and b parameters are the slopes and intercepts of the CF and NIR lines.

The accuracy of the algorithm depends upon the relative differences between the values selected for the CFs of the mineral endmembers and the Diviner CF data. The Diviner data correction described above results in CF values that represent fully mature lunar surfaces; immature surfaces have had their CF wavelength values raised to match the mature surfaces. However, there are no laboratory data on CF values for fully mature mineral endmembers to be used in the algorithm. So as an alternative, we calibrate the data set to global data from the Lunar Prospector Gamma Ray Spectrometer (LPGRS) (Prettyman et al., 2006).

Because the principal output of the algorithm is the fraction of plagioclase, and plagioclase is by far the major carrier of aluminum in the lunar crust, we will use Lunar Prospector GRS measurements of aluminum as the reference against which the output of our algorithm is measured and adjust its inputs to maximize the consistency of our results and the LPGRS measurement of alumina. We estimate alumina (Al_2O_3) for each pixel from the plagioclase fraction, where $Al_2O_{3lunar} = \text{plagioclase fraction} * Al_2O_{3plagioclase}$. There are variations in aluminum content with plagioclase composition, but in the highland crust as represented by the Apollo samples, the average composition of plagioclase is $An_{97} \pm An_{0.8}$ (Heiken et al., 1991, Table A5.7) based on the anorthite content of plagioclase in ferroan anorthosites. This corresponds to a stoichiometric alumina content of 36.1 wt. % ± 0.3 . We convert our Diviner-Multiband Imager-derived plagioclase fraction to alumina by multiplying the plagioclase fraction by this average ferroan anorthosite alumina content. We force Diviner-MI derived plagioclase global abundance so that derived alumina match those of Lunar Prospector GRS. Owing to the presence of both low aluminum, low plagioclase maria and high aluminum, high plagioclase highlands, there is a spread of alumina values across the Moon, and comparison of global values should match not only the mean aluminum content, but also the slope of the correlation, which should be 1:1. Naturally this comparison assumes the Lunar Prospector GRS measurements are correct

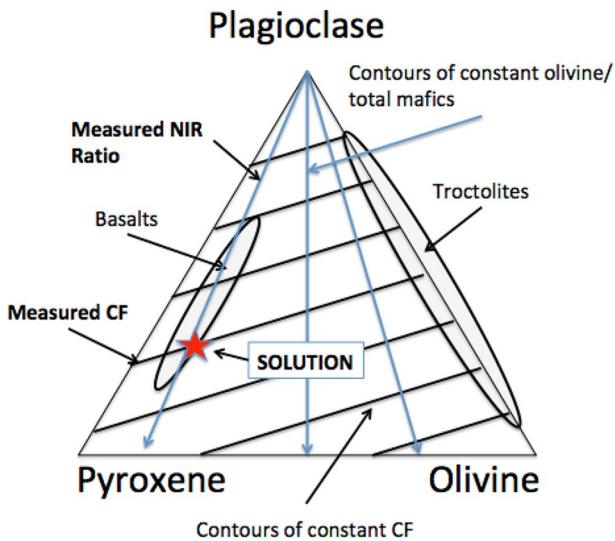


Figure 11. The Christiansen Feature (CF) ambiguity is resolved by incorporating the olivine to total mafic ratio. The “measured NIR ratio” and the “measured CF” values intersect at “Solution” (red star) on this diagram to produce a unique solution. In this case the abundance of pyroxene excluded other solutions and result in a basaltic composition.

in absolute abundance within their stated noise. We optimize the Diviner-MI calibration to match the mean LPGRS alumina and cause the slope of the correlation to be close to 1. The Diviner CF data (sampled at 32 pixels per degree) were filtered to match the spatial resolution of the much lower resolution Lunar Prospector GRS data set used here (1 pixel per 5°).

The algorithm adjusts four variables: a global shift of the mature CF position to an estimated fully immature value, and the CF values of the three mineral endmembers. The objective function is the correlation and average absolute difference of the Lunar Prospector GRS alumina data and the estimated alumina derived from the plagioclase calibration.

We begin with assigning the initial endmember CFs of anorthite, pyroxene, and olivine as 7.84 (Donaldson Hanna et al., 2014), 8.22 (Shirley and Glotch 2018), and 8.76 μm (Donaldson Hanna et al., 2017) respectively, and a global mature to immature CF shift of 0.2 μm . We found in our experimentation that the slope of the correlation between our estimated alumina and the LP measurements was very strongly influenced by CF position of the olivine, and to a lesser degree the CF position of the plagioclase, and the CF position of the pyroxene had the least effect. The final optimization gave rise to values different than those of the initial values but close to values in other publications, so we ultimately elected to use published values that were near the optimized solution,

and allow the global CF shift to absorb some of the residual error. The final CF positions used in this work are given in Table 1. The shift applied to the mature CF value is 0.18 μm to shorter wavelengths; this is our estimate of the average shift of immature lunar surface material to the longer wavelengths of fully mature surfaces. The final correlation of Diviner-Multiband Imager alumina versus Lunar Prospector GRS alumina is shown in Figure 13.

We estimate the precision of the mineral data by taking a relatively large (1,000 \times 1,000 km) area in the farside highlands (latitude -23.11 to -7.49 , longitude -148.75 to -117.49) that appears to be regionally uniform, but displays artifacts such as orbit to orbit striping and uncompensated space weathering artifacts. The 1-sigma variation within that region is 7.5 wt. % in plagioclase content, 6.8 wt. % in pyroxene content, and 6.9 wt.% in olivine content and we take these values as the uncertainty in mineral abundance. The accuracy of the data is tied to that of the Prettyman et al. (2006) estimate of aluminum content.

They do not directly cite an accuracy, but inspection of their Figure 29a shows the LPGRS data appear to closely bracket the aluminum content of a large sample of lunar soils and meteorites, with an error we estimate on the order of 1 wt. % Al_2O_3 absolute. This corresponds to about 3 wt.% in absolute plagioclase abundance.

We can assess to a degree how well we have captured the correct CF and plagioclase contents by leveraging NIR mineralogical analyses of the Moon. An indicator of the presence of relatively pure plagioclase outcrops is when the plagioclase absorption near 1,250 nm has an intensity greater than the mafic mineral absorption near 1,000 nm. Cheek and Pieters (2014) showed that this condition is always met when the abundance of mafic minerals is <2 wt%, and the onset of this condition occurs at abundances between 2 and 5 wt%. Cheek and Pieters (2014) prepared mixtures of pyroxenes and plagioclase at 98 and 95 wt.% plagioclase, and showed that at 98 wt%, the plagioclase trace iron band is stronger than the mafic absorption near 1,000 nm, but the reverse was true at 95% plagioclase. Therefore the onset of this condition is somewhere between 95%

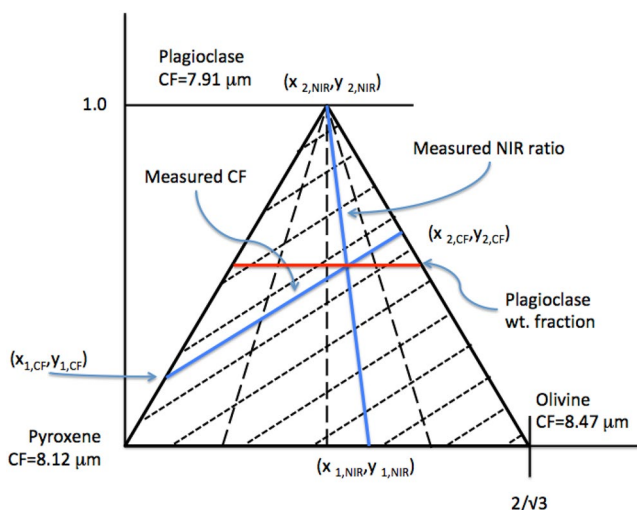


Figure 12. Recasting the ternary diagram and CF and NIR loci in a Cartesian framework. CF, Christiansen Feature.

Mineral	Value (μm)	Lab analog
Anorthite	7.81	Donaldson Hanna et al. (2012a)
Pyroxene	8.13 (average of augite and enstatite)	Donaldson Hanna et al. (2012b)
Olivine	8.47	Arnold et al. (2016)

and 98% plagioclase. Using data from Multiband Imager, we isolated the region of Orientale basin that has extensive anorthosite deposits (Ohtake et al., 2009; Yamamoto et al., 2012; Cheek et al., 2013). Removing a continuum defined by the bands at 750 and 1,550 nm, we found all pixels that had minima relative to that continuum at 1,250 nm, that is, had plagioclase iron features stronger than pyroxene features. The CF of those pixels has a mode of 7.93 μm , similar to the values found by Donaldson Hanna et al. (2012a, 2012b), and slightly longer than our pure mineral endmember, with a distribution with its half heights at 7.9 and 7.99 μm (Figure 14a). In terms of plagioclase, the mode of the histogram of this location is at 93 wt. % plagioclase, with half maxima at 80 and 101 wt% plagioclase (Figure 14b). The distribution of the MI pixels with the 1,250 minima show clear evidence of orbit to orbit calibration issues as discussed in the Data section, so perfect consistency is not expected, but the spatial distribution of areas with greater than 95% plagioclase (Figures 15a and 15b) and those with NIR band minima at 1,250 μm shows good correspondence of locations lending confidence to our methodology. We also note that plagioclase-rich regions dominated by shocked plagioclase (Bruckenthal & Pieters, 1984) lacking a band at 1,250 nm would show high abundance values to the CF-MI algorithm, but not be flagged as high plagioclase in comparing 1 μm and 1,250 nm band depths. Vitriified plagioclase shows the same CF as crystalline plagioclase (Nash & Salisbury, 1991), so the algorithm's sensitivity to plagioclase is immune to shock.3.

3. Results

3.1. CF Results

Since its introduction, the Diviner CF data set has provided a unique view of the Moon that reveals its most basic silicate mineralogy: the relative abundance of felsic and mafic material. The correction for space weathering sharpens this view by reducing the clutter introduced by space exposure. The global scale (Figure 8) reveals the basic mare-highland distinction, and the mafic anomaly of South Pole Aitken Basin is prominent. Cryptomaria are revealed as regional mafic anomalies, often near exposures of mare basalt. Local anomalies reveal concentrations of feldspar often concentrated in basin rings, and present frequently in smaller exposures in the farside highlands not associated with basin structures. Difficult to discern at this scale, but the silicic anomalies are present and show very short CF positions on high resolution inspection (see below). What are absent are prominent extensive ultramafic anomalies that could represent the long-hoped for exposures of lunar mantle, possibly revealed by impact basins, though mantle material may be diluted in the basin formation process (Moriarty et al., 2020). However, we will show a possible exposure of dunite in Moscoviense Basin (see below).

The distribution of CF values corrected for space weathering to an extent mirrors the distribution of FeO, itself corrected for space weathering, making compositional anomalies that deviate from the FeO-CF correlation difficult to discern. Lucey et al. (2017) showed that the high correlation between CF (uncorrected) and albedo was strongly violated by both silicic anomalies and olivine-rich locations. The albedo of the Moon, and

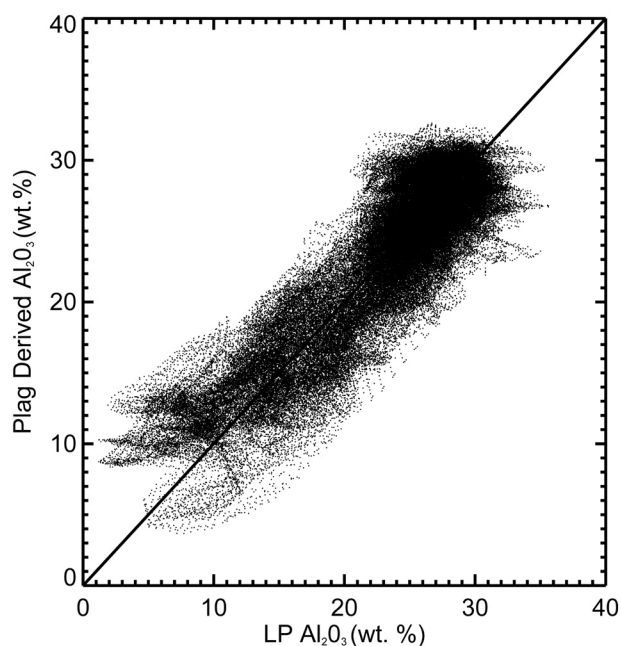


Figure 13. Correlation between Diviner-MI derived alumina and Lunar Prospector alumina derived from the plagioclase calibration following methods described in the text.

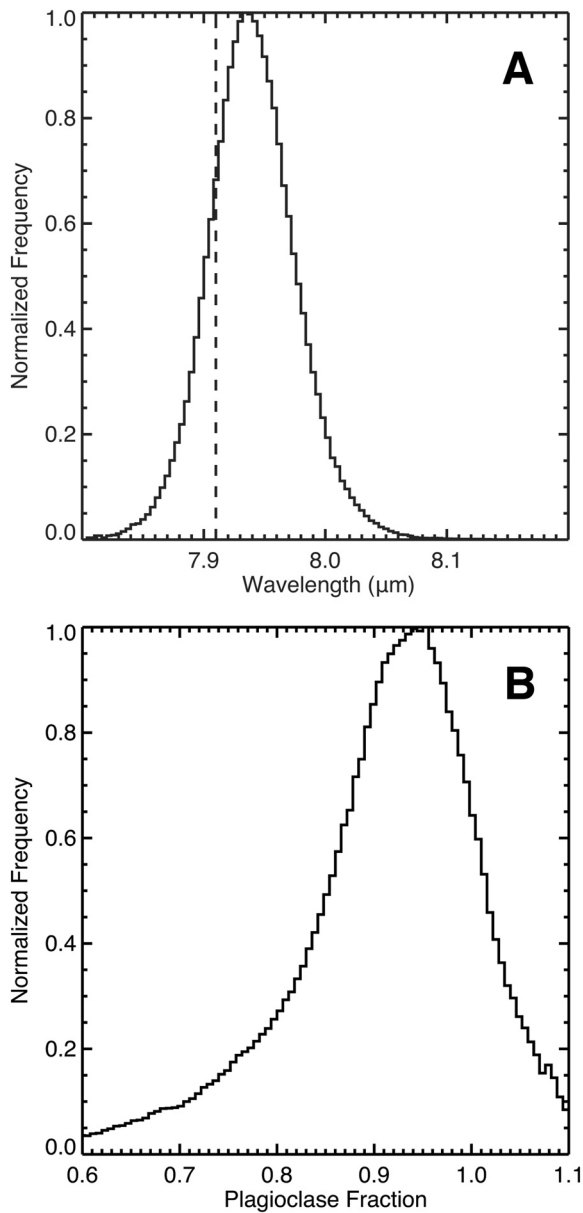


Figure 14. (a) Histogram of CF values for all pixels in the Orientale region with minima at 1.25 μm relative to a continuum defined at 750 and 1550 nm in Kaguya Multiband Imager data. Vertical line is the CF position for Jackson crater in uncorrected CF data (Donaldson Hanna et al., 2014). (b) Histogram of derived plagioclase values for pixels with near-IR minima at 1.25 μm . CF, Christiansen Feature.

the CF, is largely driven by mixtures of pyroxene and plagioclase feldspar; if a component is present with a CF very different than pyroxene or plagioclase at the same albedo, then it falls off the correlation between albedo and uncorrected CF.

We show that a similar effect is present between NIR-derived FeO (which has space weathering largely removed) and space weathering-corrected CF that reveals compositional anomalies. A compositional anomaly is one that has a CF position that differs from typical lunar behavior (largely governed by plagioclase-pyroxene mixtures) at a particular FeO content. To compute the anomaly we scale the FeO map so that the overall correlation between corrected CF and scaled FeO is 1:1:

3.2. Scaled FeO = FeO*.013 + 8.1

We then difference the corrected CF and scaled FeO to reveal locations that deviate from the overall correlation of FeO and corrected CF. The result is shown in Figure 16. This image shows that mare highland differences (and SPA) have largely been removed, revealing a host of weak anomalies at a range of scales. The most prominent negative anomalies (CF position is shorter than expected for the FeO content) are at the silica rich locations; we will examine them in more detail shortly. This parameter complements the spectral parameter called the “concavity index” that detects silicic anomalies based on their unique spectral properties in Diviner 3-band infrared color data (Glotch et al., 2011).

A prominent positive anomaly (CF position is longer than expected for the FeO content) is present on and near the rings of Moscoviense Basin on the lunar farside. In this case the CF is longer than other locations with similar FeO contents. Olivine outcrops are known to occur at Moscoviense and abundant olivine is consistent with the positive anomaly. We examine this location in greater detail here.

Moscoviense is an approximately 650-km diameter multiring basin that exhibits complex morphology and a wide-ranging volcanic history (Thaisen et al., 2011). Mare Moscoviense, within its 275 km inner ring, features compositionally diverse basalts with a wide-range of ages (Morota et al., 2009). The basin’s elongated rings and discontinuous ejecta deposits, coupled with some of the thinnest crust on the Moon, record a complex and poorly understood basin formation. Gravity data suggests that Moscoviense may actually be a double basin, the result of two impacts with nearly the same impact center (Ishihara et al., 2011). The inner ring has been observed to contain unique kilometer-scale mafic mineral exposures that are suggestive of magmatic intrusions into the lower crust, including Mg-spinel, olivine-free pyroxene, and pyroxene-free olivine (Pieters et al., 2011).

In the corrected CF image of the basin (Figure 17a), clear positive anomalies are present along the north-western rim adjacent to the maria and cropping out in moderate sized craters within the maria near the northern rim that may expose basement material. High values are also observed along the southwestern rim, in an arc extending from the southern rim partly surrounding a weak FeO high, and in the southern wall of the 22 km crater Titov within the maria. In the decorrelated image (Figure 17b) the distribution is clearer and the anomalous material extends diffusely away from the more prominent anomalies. Most of the prominent anomalies have been previously identified as olivine-bearing; here we can assess the rock type. First, isolating the anomalous areas, most of them have plagioclase contents that are clearly anortho-

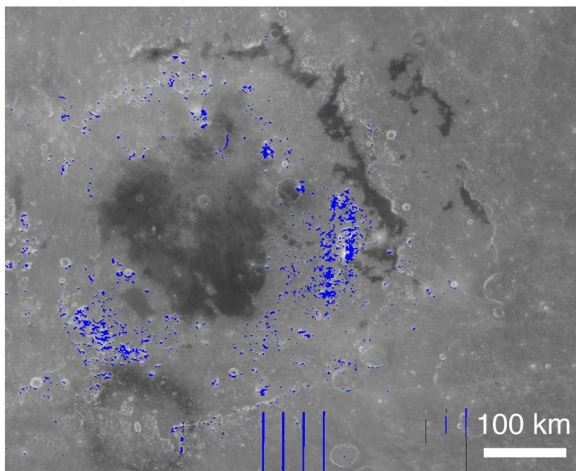
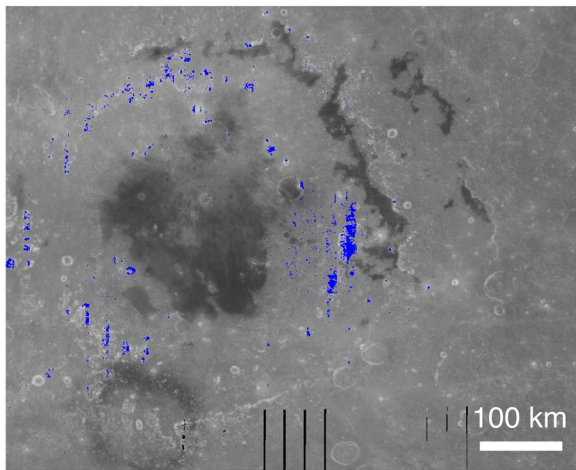


Figure 15. (a) Location of pixels in the Orientale region with minima at 1.25 μm relative to a continuum defined at 750 and 1,550 nm in Kaguya Multiband Imager data. (b) Location of pixels with >95 wt.% plagioclase from the calibration in this work.

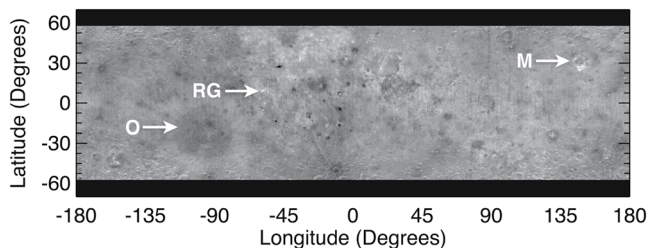


Figure 16. Result of decorrelating CF corrected for space weathering, and FeO. Mare highland differences are muted, and bright and dark anomalies are highlighted. Light and dark anomalies indicate a CF position that differs from predicted by the FeO content. The more extreme dark anomalies are silica-rich locations, while the more extreme bright anomalies can be due to excess olivine (as at Moscoviense) or anomalous space weathering as at Reiner Gamma. More subtle anomalies could be due to second order composition influences in either the CF or FeO data sets. RG: Reiner Gamma Formation. O: Orientale Basin. M: Moscoviense Basin. CF, Christiansen Feature.

A sitic; at this scale the material appears to be troctolite (Figure 18). There are a number of pixels, especially at the south wall of Titov, that extend to lower values near 20% plagioclase by weight. This location is a good candidate for possible exposures of dunite that may be revealed in mineral maps at full Diviner resolution, once calibrated to the level of the data presented here.

The decorrelation technique is also effective at isolating silica-rich regions, and identifying new ones. These features show negative anomalies, meaning that the CF position is shorter than other portions of the Moon with those FeO values. For example, a mixture of pyroxene and feldspar would give rise to some particular FeO content and CF value; silica rich regions have CFs shorter than any pyroxene-feldspar mixture sharing the same FeO content.

Figure 19 shows the decorrelation image for the Oceanus Procellarum region that features a nest of silica-rich exposures. At our 1 km resolution, we clearly identify 11 anomalies that appear to host silica-rich material of which six were previously noted as silicic (the south rim of Aristarchus crater, Mons Hansteen, Lassell Massif, the Gruithuisen Domes by Glotch, Lucey, et al. (2010), the Mairan Domes by Glotch et al. (2011), Lalande crater by Li et al. (2017), and Wolf crater by Greenhagen et al. (2017), one was dismissed by Glotch, Lucey, et al., 2010 (Mons Rhiphaeus) but this was due to incomplete coverage by Diviner at the time of writing, and three have not be previously noted (Kepler, Bessarion, and Gambert A). Figure 20 shows enlarged versions of the 11 sites. Figure 21 shows profiles of corrected CF through the portion of the anomalies with the shortest CF features. The newly identified anomalies are associated with relatively unweathered craters with strong variations in uncorrected CF due to space weathering that tend to obscure the short wavelength of the feature.

3.3. Abundance and Distribution of Major Lunar Minerals

We can derive the abundance of all three major lunar silicates (plagioclase, olivine, and pyroxene) from the ratio of olivine to mafic minerals derived from Lemelin et al. (2015), and the plagioclase we derived above from:

$$\text{Olivine} = \frac{(1 - \text{Plagioclase}) * \text{Olivine}_{\text{Lemelin}}}{(\text{Olivine}_{\text{Lemelin}} + \text{Pyroxene}_{\text{Lemelin}})}, \quad (17)$$

$$\text{Pyroxene} = 1 - (\text{Plagioclase} + \text{Olivine}). \quad (18)$$

This results in the abundance of plagioclase, pyroxene, and olivine at 1 km resolution between latitudes of 62°N and 62°S where data quality is highest. The lunar surface comprises three major physiographic terranes that feature separate histories and surface expression: the Feldspathic Highlands Terrane, the Procellarum KREEP Terrane and the South Pole Aitken Terrane (Jolliff et al., 2000). As a practical matter for surface remote sensing, the mare surface is a fourth province. Figure 22 shows the histograms of distribution of plagioclase, pyroxene, and olivine of the three terranes and the surface of the maria. The mode of plagioclase content in the Feldspathic Highlands Terrane is about 85 wt. %

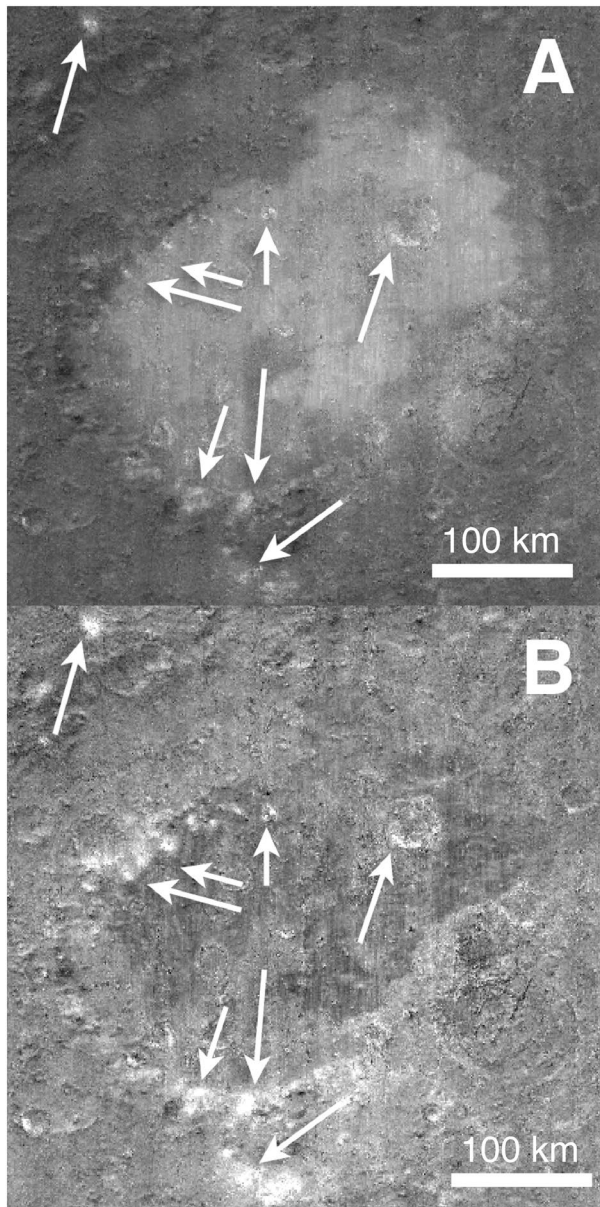


Figure 17. (a) CF of Moscoviense Basin, corrected for space weathering. Prominent CF bright (long wavelength) anomalies occur near the basin ring, and at a crater to the northwest. Stretch is from 6.7 to 9.6 μm . (b) CF of Moscoviense Basin, corrected for space weathering and decorrelated from FeO. The CF anomalies are shown to affect a larger area around their main exposures. CF, Christiansen Feature.

boundaries between highland and mare exposures (Figure 23). The prominent albedo, iron, and plagioclase anomaly of South Pole Aitken is very subdued, with olivine contents only slightly above the regional highland background. Olivine appears to “false alarm” on pyroclastic deposits with high values at many prominent exposures; the spectral similarity of glass and olivine are likely spoofing the near-IR detection algorithm. It is important to avoid interpretation of MI-based olivine mineral abundances in the vicinity of known or suspected pyroclastic deposits (e.g., Moriarty & Petro, 2020). However, the background volcanic glass abundance in the lunar maria is only a few percent based on analyses of Apollo 11 and 12 soils (Taylor

and the balance is mostly pyroxene. The maria show an approximately equal amount of plagioclase and pyroxene consistent with their basaltic nature. The mafic nature of the South Pole Aitken and Procellarum KREEP terranes is expressed in their mafic content intermediate between the Feldspathic Highlands Terrane and the lunar maria.

The Feldspathic Highlands Terrane includes most of the lunar surface and is characterized by high albedo, low iron, and thorium concentrations. This terrane appears to represent the remains of the original lunar crust formed from the crystallization of the lunar magma ocean, though highly modified by over 4 billion years of impacts. Within the context of the Lunar Magma Ocean Hypothesis, the lunar crust formed by plagioclase flotation on a relatively dense residual liquid to form the famous anorthosites. However, it has long been recognized that the average highlands crust (away from the more mafic terranes) is too iron rich and too aluminum poor to be composed of pure anorthosite by that rock type’s formal definition as containing less than 10% mafic minerals (olivine and pyroxene) by volume. On the basis of X-ray remote sensing, Taylor (1982) suggested the highland surface was anorthositic, but not anorthosite. Spudis and Davis (1986) and Davis and Spudis (1985) also recognized this mafic enrichment and suggested the average surface composition was “gabbroic anorthosite.” Similarly, Korotev et al. (2003) came to a similar conclusion from the composition of feldspathic lunar meteorites featuring very low incompatible element concentrations indicating an origin far from the anomalous Apollo sampling zone; suggested a composition of anorthositic norite based on the classification of Stöfler et al. (1980).

The results here are consistent with that prior work. Figure 22 shows the histograms of distribution of plagioclase, pyroxene, and olivine of the three terranes and the surface of the maria. The mode of the Feldspathic Highlands Terrane is about 85 wt. %. Anorthosites are defined on a volume percent basis, and using densities of 2.73, 3.22, and 3.33 g/cc for plagioclase, pyroxene, and olivine, respectively, the mode of the histogram is about 87 vol. %; much of the feldspathic highland crust is more mafic than anorthosite as strictly defined.

The global distribution of plagioclase offers few surprises (Figure 23). The highest abundances are on the farside as implied by Lunar Prospector GRS measurements of aluminum (and iron) (Prettyman et al., 2006); lowest regional values are found in the lunar maria, especially the young basalts of Oceanus Procellarum and western Imbrium. Notable high values appear associated with rings of Orientale, Nectarus, Humorum, with local anomalies, including those at Copernicus, Humboldt, and Gagarin.

The distribution of olivine closely follows the distribution of the maria, with low and relatively uniform values in the highlands and sharp

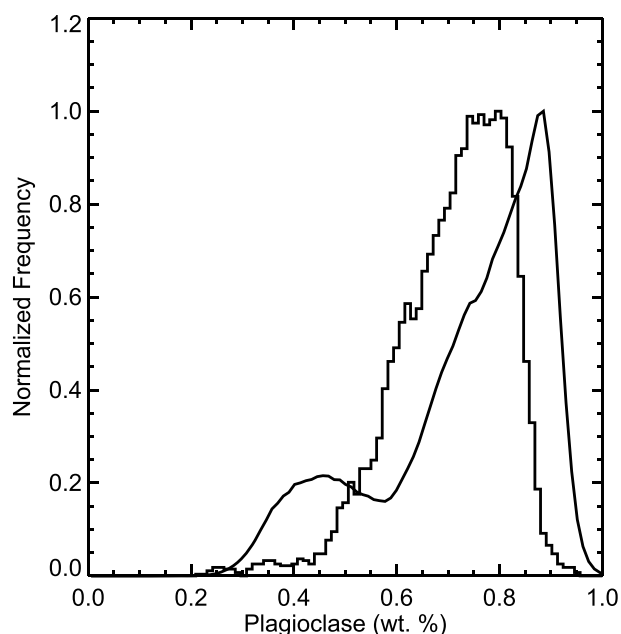


Figure 18. Histogram of plagioclase content for the region shown in Figure 17a (smooth line), and of the anomalous areas revealed in the decorrelation images shown in Figure 17b (histogram style stepped line). Most anomalous pixels contain considerable plagioclase so these olivine-rich exposures are troctolite. A few pixels (largely from the south rim of Titov) show lower plagioclase content and may be hinting at a mantle exposure that may be revealed at higher resolution.

average highlands crust (away from the more mafic terranes) is too iron-rich and too aluminum-poor to be composed of pure anorthosite by that rock type's formal definition as containing less than 10% mafic minerals (olivine and pyroxene) by volume. On the basis of X-ray remote sensing, Taylor (1982) suggested the highland surface was anorthositic, but not anorthosite. Spudis and Davis (1986) and Davis and Spudis (1985) also recognized this mafic enrichment and suggested the average surface composition was "gabbroic anorthosite." Similarly, Korotev et al. (2003) came to a similar conclusion from the composition of feldspathic lunar meteorites featuring very low incompatible element concentrations indicating an origin far from the anomalous Apollo sampling zone; suggested a composition of anorthositic norite based on the classification of Stöffler et al. (1980).

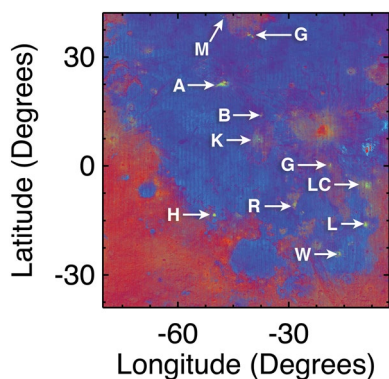


Figure 19. Silica anomalies of the Oceanus Procellarum Region. In this rendition yellows and light greens are silica-rich anomalies, reds are low FeO and blue are high FeO. M, Mairan Domes; G, Gruithuisen Domes; A, Aristarchus Crater; B, Bessarion Crater; K, Kepler Crater; H, Mons Hansteen; R, Montes Riphaeus; LC, Lalande Crater; L, Lassell Massif; W, Wolf Crater; G, Gambart A crater.

et al. 1996, 2001), so olivine abundance above that level are likely due to the mineral and not due to glass contamination.

While relatively abundant olivine appears largely associated with mare deposits and cryptomaria, enhanced pyroxene is observed both in the maria and in the more mafic portions of the lunar highlands: the South Pole Aitken Terrane and the Procellarum KREEP Terrane. Interestingly, boundary between the low FeO Mare Frigoris and the surrounding highlands is indistinct in the pyroxene map. This may be a coincidence, where the two unit share pyroxene abundances, but the balance of the highlands is plagioclase whereas the balance of the mare surface is shared between olivine and plagioclase.

4. Discussion

At the global level, these results are tied to the elemental measurements by Lunar Prospector GRS, so provide no new constraints beyond extension to higher spatial resolution. However, the volume abundance of plagioclase and pyroxene underscore a fundamental problem brought into focus by Crites et al. (2015): the feldspathic portions of the crust are somewhat too mafic to be composed dominantly of anorthosite. The Feldspathic Highlands Terrane includes most of the lunar surface and is characterized by high albedo, low iron, and thorium concentrations. This terrane appears to represent the remains of the original lunar crust formed from the crystallization of the lunar magma ocean, though highly modified by over 4 billion years of impacts. Within the context of the Lunar Magma Ocean Hypothesis, the lunar crust formed by plagioclase flotation on a relatively dense residual liquid to form the famous anorthosites. However, it has long been recognized that the

The results here are consistent with that prior work. Figure 22 shows the histograms of distribution of plagioclase, pyroxene, and olivine of the three terranes and the surface of the maria. The mode of the Feldspathic Highlands Terrane is about 85 wt. %. Anorthosites are defined on a volume percent basis, and using densities of 2.73, 3.22, 3.33 g/cc for plagioclase, pyroxene, and olivine, respectively, the mode of the histogram is about 87 vol. %; much of the feldspathic highland crust is more mafic than anorthosite as strictly defined.

Ohtake et al. (2009) and Yamamoto et al. (2012) argued that anorthosite is dominant at depths below a few kilometers, but that contention is based on the detection of ubiquitous anorthite in central peaks and other relevant deposits, not a comprehensive quantitative assay. Quantitative

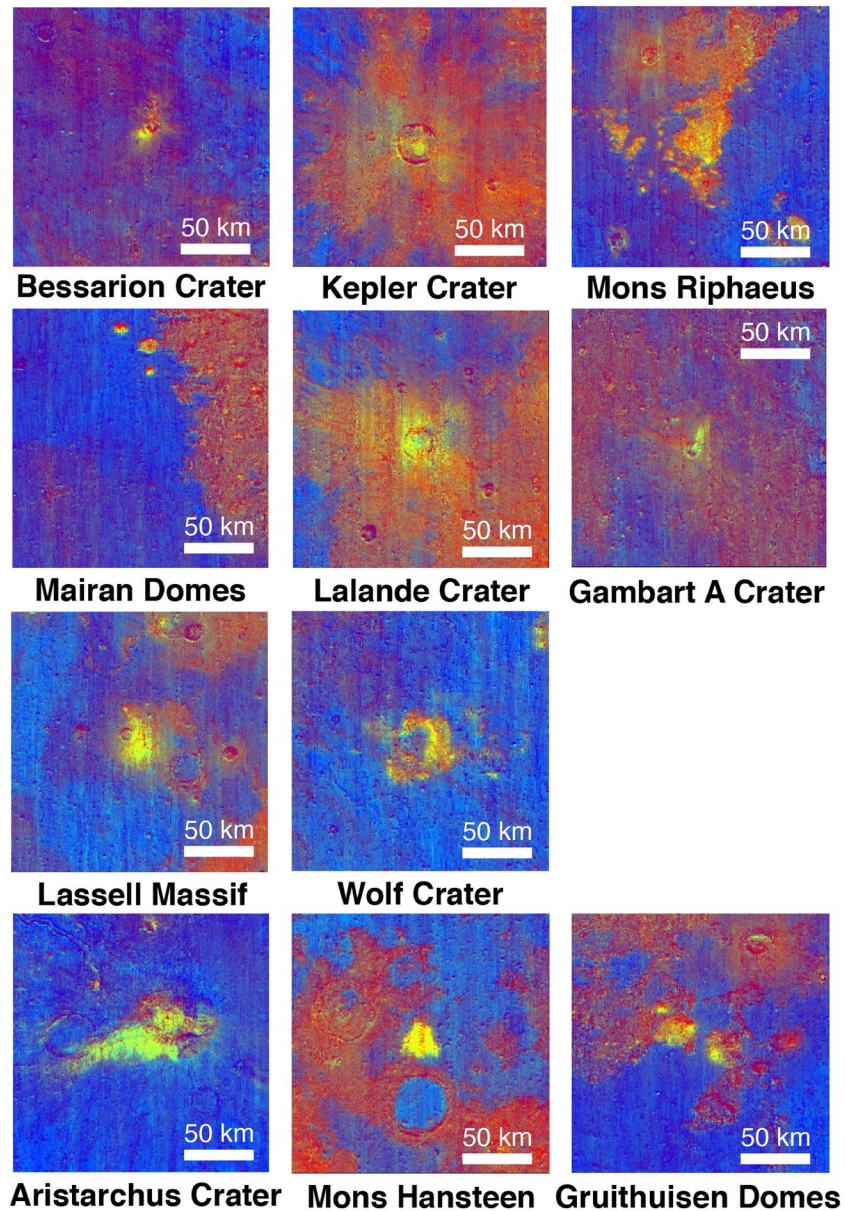


Figure 20. Thumbnail closeups of the 11 silica rich regions discussed in the text.

surveys of central peak mineralogy do not reveal obvious consistent variation in plagioclase abundance with depth (Cahill et al., 2009; Lemelin et al., 2015). The surface mafic component does not exclude detection of abundant anorthosite at depth, and with almost 90% of the crust composed of feldspar, anorthosite ought to be a common rock throughout the crust, and does not erode the arguments and need for a magma ocean with an anorthosite flotation crust. But a substantial portion of the pyroxene must have been emplaced outside that process.

Crites et al. (2015) noted this excess mafic component and explored three alternatives: that the typical anorthosite that makes up the crust is more mafic than appears represented in the sample collection; that very early volcanic products are mixed into the crust; that a mantle derived mafic component is present to drive up the mafic content. They leaned against the "mafic anorthosite" hypothesis based on the ubiquity of "pure anorthosites" in basin rings and central peaks that suggest very low mafic anorthosite is at least very common (though more mafic anorthosite may be indistinguishable from mixtures). They also leaned against

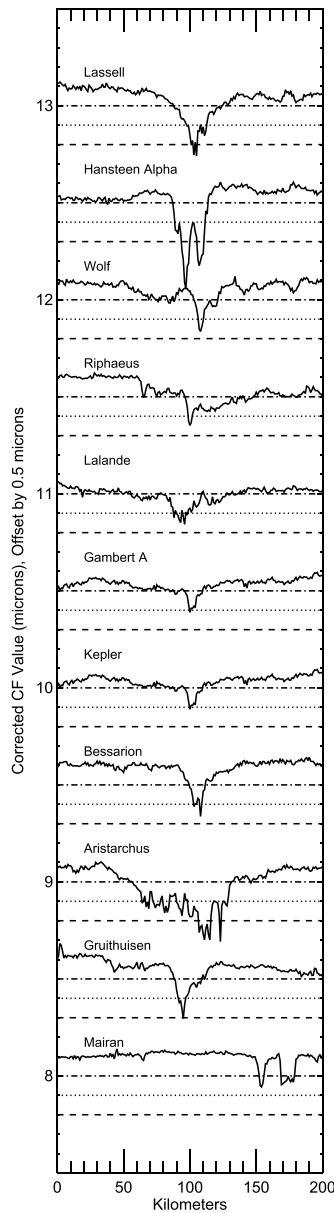


Figure 21. East-West profiles of space weathering corrected CF for the 11 anomalies discussed in the text. The dashed lines are at 7.8, 7.9, and 8 μm . CF, Christiansen Feature.

the “volcanic” hypothesis because about 30 wt% of the crust would be required to be volcanic to account for the excess mafic component, and they reasoned that this would be represented by abundant evidence in the sample collection. They favored the mantle contaminant concept and showed the contributions by the known basins assuming simple excavation models were roughly consistent with the required masses. Our work, not materially changing prior estimates of the abundance of the mafic component, does not alter the assumptions within which Crites et al. (2015) operated.

Some features in the data presented are unexpected. In the decorrelated CF and FeO image shown in Figure 16, the material within the Cordillera Ring of Orientale is prominent as a circular negative anomaly. We do not suggest that this feature is due to enhanced silica; both the CF and FeO parameters can be affected by numerous secondary compositional effects, silica or olivine are just the most extreme known. Rather, the Orientale feature indicates that there is a consistent spectral difference between the ejecta and its surroundings, and that spectral difference must be due to some subtle compositional or physical difference that affects either the CF or the near-IR bands from which the FeO data are derived. The distal ejecta is distinct from material within the sharp boundary of the Cordillera Ring, and displays an irregular boundary around the basin. The outer deposit appears to correspond closely to Facies B of Morse et al. (2018), whereas all the deposits within the Cordillera Ring appear similar at this scale. This anomaly shows that some process has altered the spectral properties of the material within and without the Cordillera Ring to produce a measurable compositional signal.

The growing list of widespread silicic anomalies, including these new features show that silicic material may be extensive below the mare in this region, though the modestly extended spatial range in this work does not appear to influence prior hypotheses for the origin of these features (Ashley et al., 2016; Boyce et al., 2018; Glotch et al., 2010, 2011; Jolliff et al., 2011). Additional candidates, including smaller features, are being targeted by Diviner and LROC as part of the LRO fourth extended science mission (2019–2023).

Finally, the Reiner Gamma Formation, a prominent “lunar swirl” that appears to be a space weathering anomaly due the shielding effects of a strong local magnetic field, shows a prominent positive anomaly. There is no evidence from the CF or other analyses that this location has an anomalous primary composition (Glotch, Bandfield, et al., 2015), rather that the assumptions underlying the space weathering mitigations applied both to the FeO data set, and the corrected CF here, are incorrect at this unusual location.

5. Conclusions

In this study, we improved the utility of the Diviner CF data product by better removing the effect of space weathering. We combined this improved parameter with previously determined mafic mineral ratios to produce a new derivation of the abundances of plagioclase, pyroxene, and olivine, ultimately tied to the aluminum measurements of Lunar Prospector GRS. We presented the volumetric abundance of these minerals as manifest at the surface. We developed a new method for detection of silicic and ultramafic anomalies and

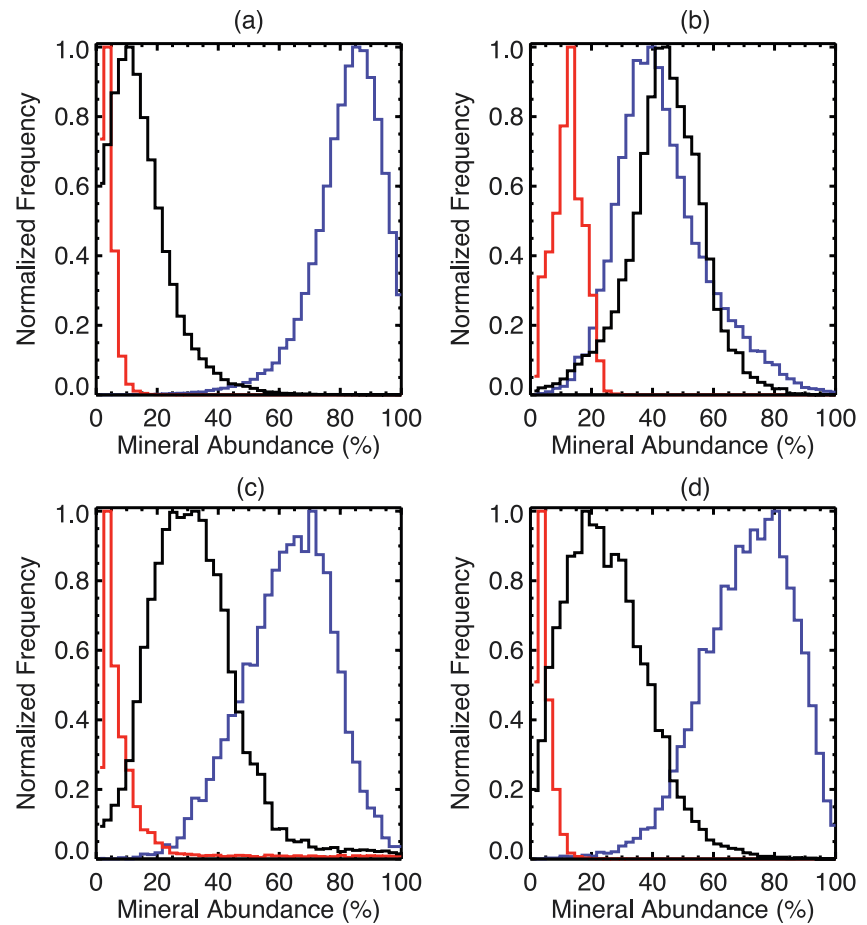


Figure 22. Histograms of the global abundances of olivine (blue), pyroxene (red) and plagioclase (black) for the Feldspathic Highlands Terrane (upper left), the maria (upper right), the South Pole Aitken Terrane (lower left) and the Procellarum KREEP Terrane (lower right). Distributions are normalized to the peak frequency of plagioclase.

used these to find new exposures of silicic material, and a candidate for an exposure of the lunar mantle at the crater Titov in Moscoviense Basin. We reminded the reader of the nagging problem of an excess mafic component of the lunar crust.

Future work will take the power of this development to applications of local-scale phenomena at the full resolution of these products, and higher resolution equivalents that exploit the maximum resolution available from the combination of data from Diviner and Multiband Imager.

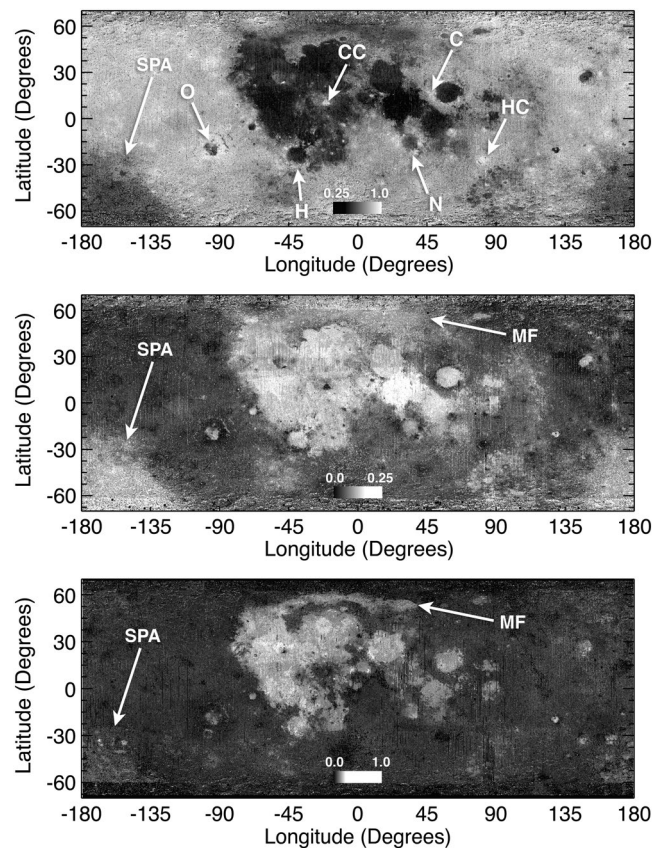


Figure 23. Maps of plagioclase, pyroxene and olivine abundances. SPA, South Pole Aitken Terrane; O, Orientale Basin; CC, Copernicus Crater; H, Humorum Basin; C, Crisium Basin ring; N, Nectaris Basin; HC, Humboldt Crater; M, Mare Frigoris.

Data Availability Statement

New data products reported here can be found at Zenodo: Greenhagen, B. T., Donaldson Hanna, K., Lucey, P. G., Bowles, N., Isaacson, P., & Milliken, R. (2021). Diviner Christiansen Feature Map. Zenodo. <http://doi.org/10.5281/zenodo.4558235> and Lucey, P. G., Greenhagen, B. T., Donaldson Hanna, K., Bowles, N., Flom, A., & Paige, D. A. (2021). Lunar Mineralogy Derived from Improved Diviner Lunar Radiometer Christiansen Feature Maps. Zenodo. <http://doi.org/10.5281/zenodo.4558194>. The mineral, optical maturity (OMAT), and FeO maps used in this work can be found at this USGS website: <https://astrogeology.usgs.gov/tools/map-a-planet>.

Acknowledgments

This work was supported by the Lunar Data Analysis Program under a grant to Benjamin Greenhagen, and by the Lunar Reconnaissance Orbiter Project's Diviner Lunar Radiometer Experiment, David A. Paige, Principal Investigator. Detailed and important reviews were provided by Tim Glotch and Daniel Moriarty and the authors thank them for their time, diligence, and collegial tone.

References

- Arnold, J. A., Glotch, T. D., Lucey, P. G., Song, E., Thomas, I. R., Bowles, N. E., & Greenhagen, B. T. (2016). Constraints on olivine-rich rock types on the Moon as observed by Diviner and M3: Implications for the formation of the lunar crust. *Journal of Geophysical Research: Planets*, *121*, 1342–1361. <https://doi.org/10.1002/2015je004874>
- Ashley, J. W., Robinson, M. S., Stopar, J. D., Glotch, T. D., Hawke, B. R., Van der Bogert, C. H., et al. (2016). The Lassell massif-A silicic lunar volcano. *Icarus*, *273*, 248–261. <https://doi.org/10.1016/j.icarus.2015.12.036>
- Boyce, J. M., Giguere, T., Mouginiis-Mark, P., Glotch, T., & Taylor, G. J. (2018). Geology of Mairan middle dome: Its implication to silicic volcanism on the Moon. *Planetary and Space Science*, *162*, 62–72.
- Bretzfelder, J. M., Klima, R. L., Greenhagen, B. T., Buczkowski, D. L., Petro, N. E., & Day, M. (2020). Identification of potential mantle rocks around the lunar Imbrium basin. *Geophysical Research Letters*, *47*(22), e2020GL090334.
- Bruckenthal, E. A., & Pieters, C. M. (1984). Spectral effects of natural shock on plagioclase feldspar. *Proceedings of the Lunar and Planetary Science Conference*, *15*, 96–97.
- Cahill, J. T., & Lucey, P. G. (2007). Radiative transfer modeling of lunar highlands spectral classes and relationship to lunar samples. *Journal of Geophysical Research*, *112*, E10007. <https://doi.org/10.1029/2006je002868>

- Cahill, J. T., Lucey, P. G., & Wieczorek, M. A. (2009). Compositional variations of the lunar crust: Results from radiative transfer modeling of central peak spectra. *Journal of Geophysical Research*, *114*, E09001. <https://doi.org/10.1029/2008je003282>
- Cheek, L. C., Donaldson Hanna, K. L., Pieters, C. M., Head, J. W., & Whitten, J. L. (2013). The distribution and purity of anorthosite across the Orientale basin: New perspectives from Moon Mineralogy Mapper data. *Journal of Geophysical Research: Planets*, *118*, 1805–1820. <https://doi.org/10.1002/jgre.20126>
- Cheek, L. C., & Pieters, C. M. (2014). Reflectance spectroscopy of plagioclase-dominated mineral mixtures: Implications for characterizing lunar anorthosites remotely. *American Mineralogist*, *99*(10), 1871–1892. <https://doi.org/10.2138/am-2014-4785>
- Conel, J. E. (1969). Infrared emissivities of silicates: Experimental results and a cloudy atmosphere model of spectral emission from condensed particulate mediums. *Journal of Geophysical Research*, *74*(6), 1614–1634. <https://doi.org/10.1029/jb074i006p01614>
- Crites, S. T., Lucey, P. G., & Taylor, G. J. (2015). The mafic component of the lunar crust: Constraints on the crustal abundance of mantle and intrusive rock, and the mineralogy of lunar anorthosites. *American Mineralogist*, *100*(8–9), 1708–1716. <https://doi.org/10.2138/am-2015-4872>
- Davis, P. A., & Spudis, P. D. (1985). Petrologic province maps of the lunar highlands derived from orbital geochemical data. *Journal of Geophysical Research*, *90*(S01), 61–74. <https://doi.org/10.1029/jb090is01p00061>
- Donaldson Hanna, K. L., Cheek, L. C., Pieters, C. M., Mustard, J. F., Greenhagen, B. T., Thomas, I. R., & Bowles, N. E. (2014). Global assessment of pure crystalline plagioclase across the Moon and implications for the evolution of the primary crust. *Journal of Geophysical Research: Planets*, *119*, 1516–1545.
- Donaldson Hanna, K. L., Greenhagen, B. T., Patterson, III, W. R., Pieters, C. M., Mustard, J. F., Bowles, N. E., et al. (2017). Effects of varying environmental conditions on emissivity spectra of bulk lunar soils: Application to Diviner thermal infrared observations of the Moon. *Icarus*, *283*, 326–342. <https://doi.org/10.1016/j.icarus.2016.05.034>
- Donaldson Hanna, K. L., Thomas, I. R., Bowles, N. E., Greenhagen, B. T., Pieters, C. M., Mustard, J. F., et al. (2012a). Laboratory emissivity measurements of the plagioclase solid solution series under varying environmental conditions. *Journal of Geophysical Research*, *117*, E11004. <https://doi.org/10.1029/2012je004184>
- Donaldson Hanna, K. L., Wyatt, M. B., Thomas, I. R., Bowles, N. E., Greenhagen, B. T., Maturilli, A., et al. (2012b). Thermal infrared emissivity measurements under a simulated lunar environment: Application to the diviner lunar radiometer experiment. *Journal of Geophysical Research*, *117*, E00H05. <https://doi.org/10.1029/2011je003862>
- Glotch, T. D., Bandfield, J. L., Lucey, P. G., Hayne, P. O., Greenhagen, B. T., Arnold, J. A., et al. (2015). Formation of lunar swirls by magnetic field standoff of the solar wind. *Nature Communications*, *6*, 6189. <https://doi.org/10.1038/ncomms7189>
- Glotch, T. D., Hagerty, J. J., Lucey, P. G., Hawke, B. R., Giguere, T. A., Arnold, J. A., et al. (2011). The Mairan domes: Silicic volcanic constructs on the Moon. *Geophysical Research Letters*, *38*, L21204. <https://doi.org/10.1029/2011gl049548>
- Glotch, T. D., Lucey, P. G., Bandfield, J. L., Greenhagen, B. T., Thomas, I. R., Elphic, R. C., et al. (2010). Highly silicic compositions on the Moon. *Science*, *329*(5998), 1510–1513. <https://doi.org/10.1126/science.1192148>
- Greenhagen, B. T., Cahill, J. T., Jolliff, B. L., Lawrence, S. J., & Glotch, T. D. (2017). Investigating evolved compositions around Wolf Crater. Paper presented at *Lunar and Planetary Science Conference 2017* (No. 1964, p. 2597).
- Greenhagen, B. T., Lucey, P. G., Bandfield, J. L., Hayne, P. O., Williams, J. P., & Paige, D. A. (2011). The Diviner Lunar Radiometer compositional data products: Description and examples. In *Lunar and Planetary Science Conference 2011* (No. 1608, p. 2679).
- Greenhagen, B. T., Lucey, P. G., Wyatt, M. B., Glotch, T. D., Allen, C. C., Arnold, J. A., et al. (2010). Global silicate mineralogy of the Moon from the Diviner Lunar Radiometer. *Science*, *329*(5998), 1507–1509. <https://doi.org/10.1126/science.1192196>
- Heiken, G. H., Vaniman, D. T., & French, B. M. (1991). *Lunar Sourcebook, a user's guide to the Moon*. Cambridge University Press.
- Henderson, B. G., & B. M. Jakosky, (1994). Near-surface thermal gradients and their effects on mid-infrared emission spectra of planetary surfaces. *Journal of Geophysical Research*, *99*(E9), 19063–19073.
- Ishihara, Y., Morota, T., Nakamura, R., Goossens, S., & Sasaki, S. (2011). Anomalous Moscoviense basin: Single oblique impact or double impact origin? *Geophysical Research Letters*, *38*, L03201. <https://doi.org/10.1029/2010gl045887>
- Jolliff, B. L., Gillis, J. J., Haskin, L. A., Korotev, R. L., & Wieczorek, M. A. (2000). Major lunar crustal terranes: Surface expressions and crust-mantle origins. *Journal of Geophysical Research*, *105*(E2), 4197–4216. <https://doi.org/10.1029/1999je001103>
- Jolliff, B. L., Tran, T. N., Lawrence, S. J., Robinson, M. S., Scholten, F., Oberst, J., et al. (2011). Compton-Belkovich: Nonmare, Silicic Volcanism on the Moon's Far Side. Paper presented at *Lunar and Planetary Science Conference* (No. 1608, p. 2224).
- Korotev, R. L., Jolliff, B. L., Zeigler, R. A., Gillis, J. J., & Haskin, L. A. (2003). Feldspathic lunar meteorites and their implications for compositional remote sensing of the lunar surface and the composition of the lunar crust. *Geochimica et Cosmochimica Acta*, *67*(24), 4895–4923. <https://doi.org/10.1016/j.gca.2003.08.001>
- Lemelin, M., Lucey, P. G., Miljković, K., Gaddis, L. R., Hare, T., & Ohtake, M. (2019). The compositions of the lunar crust and upper mantle: Spectral analysis of the inner rings of lunar impact basins. *Planetary and Space Science*, *165*, 230–243. <https://doi.org/10.1016/j.pss.2018.10.003>
- Lemelin, M., Lucey, P. G., Song, E., & Taylor, G. J. (2015). Lunar central peak mineralogy and iron content using the Kaguya Multiband Imager: Reassessment of the compositional structure of the lunar crust. *Journal of Geophysical Research: Planets*, *120*, 869–887. <https://doi.org/10.1002/2014je004778>
- Li, B., Ling, Z. C., Zhang, J., Chen, J., Liu, C. Q., & Bi, X. Y. (2017). Geological mapping of lunar crater lalande: Topographic configuration, morphology and cratering process. *The International Archives of the Photogrammetry, Remote Sensing and Spatial Information Sciences*, *42*.
- Logan, L. M., Hunt, G. R., Salisbury, J. W., & Balsamo, S. R. (1973). Compositional implications of Christiansen frequency maximums for infrared remote sensing applications. *Journal of Geophysical Research*, *78*(23), 4983–5003. doi: <https://doi.org/10.1029/jb078i023p04983>
- Lucey, P. G. (2002). Radiative transfer model constraints on the shock state of remotely sensed lunar anorthosites. *Geophysical Research Letters*, *29*(10), 124–131. <https://doi.org/10.1029/2001GL014655>
- Lucey, P. G. (2004). Mineral maps of the Moon. *Geophysical Research Letters*, *31*, L08701. <https://doi.org/10.1029/2003GL019406>
- Lucey, P. G., Blewett, D. T., Taylor, G. J., & Hawke, B. R. (2000). Imaging of lunar surface maturity. *Journal of Geophysical Research*, *105*(E8), 20377–20386. <https://doi.org/10.1029/1999je001110>
- Lucey, P. G., Greenhagen, B. T., Song, E., Arnold, J. A., Lemelin, M., Hanna, K. D., et al. (2017). Space weathering effects in diviner lunar radiometer multispectral infrared measurements of the lunar Christiansen feature: Characteristics and mitigation. *Icarus*, *283*, 343–351. <https://doi.org/10.1016/j.icarus.2016.05.010>
- Lucey, P. G., Norman, J. A., Crites, S. T., Taylor, G. J., Hawke, B. R., Lemelin, M., & Melosh, H. J. (2014). A large spectral survey of small lunar craters: Implications for the composition of the lunar mantle. *American Mineralogist*, *99*(11–12), 2251–2257. <https://doi.org/10.2138/am-2014-4854>

- Lyon, R. J. P. (1965). Analysis of rocks by spectral infrared emission (8 to 25 microns). *Economic Geology*, *60*, 715–736. <https://doi.org/10.2113/gsecongeo.60.4.715>
- Martinot, M., Flahaut, J., Besse, S., Quantin-Nataf, C., & van Westrenen, W. (2018). Compositional variations in the vicinity of the lunar crust-mantle interface from Moon mineralogy mapper data. *Journal of Geophysical Research: Planets*, *123*, 3220–3237. <https://doi.org/10.1029/2018je005744>
- Melosh, H. J., Kendall, J., Horgan, B., Johnson, B. C., Bowling, T., Lucey, P. G., & Taylor, G. J. (2017). South Pole-Aitken basin ejecta reveal the Moon's upper mantle. *Geology*, *45*(12), 1063–1066. <https://doi.org/10.1130/g39375.1>
- Moriarty, D. P., & Petro, N. E. (2020). Mineralogical diversity of the Von Karman region and the validity of Mantle-derived Olivine detections by Chang'E 4/Yutu-2. In *Lunar and Planetary Science Conference* (No. 2326, p. 2660).
- Moriarty, D. P., Pieters, C. M., & Isaacson, P. J. (2013). Compositional heterogeneity of central peaks within the South Pole-Aitken Basin. *Journal of Geophysical Research: Planets*, *118*(11), 2310–2322. <https://doi.org/10.1002/2013je004376>
- Moriarty, D. P., Watkins, R. N., Valencia, S. N., Kendall, J. D., Evans, A. J., Dygert, N., & Petro, N. E. (2020). Evidence for a stratified upper mantle preserved within the south Pole—Aitken basin. *Journal of Geophysical Research: Planets*, *121*, e2020JE006589.
- Morota, T., Haruyama, J., Honda, C., Ohtake, M., Yokota, Y., Kimura, J., et al. (2009). Mare volcanism in the lunar farside Moscoviense region: Implication for lateral variation in magma production of the Moon. *Geophysical Research Letters*, *36*, L21202. <https://doi.org/10.1029/2009gl040472>
- Morse, Z. R., Osinski, G. R., & Tornabene, L. L. (2018). New morphological mapping and interpretation of ejecta deposits from Orientale Basin on the Moon. *Icarus*, *299*, 253–271. <https://doi.org/10.1016/j.icarus.2017.08.010>
- Nakamura, R., Matsunaga, T., Ogawa, Y., Yamamoto, S., Hiroi, T., Saiki, K., et al. (2009). Ultramafic impact melt sheet beneath the South Pole-Aitken basin on the Moon. *Geophysical Research Letters*, *36*(22), L22202. <https://doi.org/10.1029/2009gl040765>
- Nash, D. B., & Salisbury, J. W. (1991). Infrared reflectance spectra (2.2–15 μm) of plagioclase feldspars. *Geophysical Research Letters*, *18*(6), 1151–1154. <https://doi.org/10.1029/91gl01008>
- Ohtake, M., Matsunaga, T., Haruyama, J., Yokota, Y., Morota, T., Honda, C., et al. (2009). The global distribution of pure anorthosite on the Moon. *Nature*, *461*(7261), 236–240. <https://doi.org/10.1038/nature08317>
- Pieters, C. M., Besse, S., Boardman, J., Buratti, B., Cheek, L., Clark, R. N., et al. (2011). Mg-spinel lithology: A new rock type on the lunar farside. *Journal of Geophysical Research*, *116*, E00G08.
- Pieters, C. M., & Wilhelms, D. E. (1985). Origin of olivine at Copernicus. *Journal of Geophysical Research*, *90*(S02), C415–C420. <https://doi.org/10.1029/jb090is02p0c415>
- Prettyman, T. H., Hagerty, J. J., Elphic, R. C., Feldman, W. C., Lawrence, D. J., McKinney, G. W., & Vaniman, D. T. (2006). Elemental composition of the lunar surface: Analysis of gamma ray spectroscopy data from lunar prospector. *Journal of Geophysical Research*, *111*, E12007. <https://doi.org/10.1029/2005je002656>
- Runyon, K. D., Moriarty, III, D. P., Denevi, B. W., Greenhagen, B. T., Morgan, G., Young, K. E., et al. (2020). Impact Melt facies in the Moon's Crisium basin: Identifying, characterizing, and future radiogenic dating. *Journal of Geophysical Research: Planets*, *125*, e2019JE006024. <https://doi.org/10.1029/2019je006024>
- Ryder, G., & Wood, J. A. (1977). Serenitatis and Imbrium impact melts: Implications for large-scale layer in the lunar crust. *Proceedings of the 8th Lunar Science Conference*, (pp. 655–668).
- Salisbury, J. W., Basu, A., & Fischer, E. M. (1997). Thermal infrared spectra of lunar soils. *Icarus*, *130*(1), 125–139. <https://doi.org/10.1006/icar.1997.5809>
- Salisbury, J. W., Walter, L. S., Vergo, N., & d'Aria, D. M. (1991). *Infrared (2.1–25 mm) spectra of minerals* (p. 267).
- Shirley, K., & Glotch, T. (2018). Effects of visible Albedo on mid-infrared spectra under simulated lunar environment as compared to diviner lunar radiometer. In *European Planetary Science Congress*.
- Song, E., Bandfield, J. L., Lucey, P. G., Greenhagen, B. T., & Paige, D. A. (2013). Bulk mineralogy of lunar crater central peaks via thermal infrared spectra from the diviner lunar radiometer: A study of the Moon's crustal composition at depth. *Journal of Geophysical Research: Planets*, *118*, 689–707. <https://doi.org/10.1002/jgre.20065>
- Spudis, P. D., & Davis, P. A. (1986). A chemical and petrological model of the lunar crust and implications for lunar crustal origin. *Journal of Geophysical Research*, *91*(B13), E84–E90. <https://doi.org/10.1029/jb091ib13p00e84>
- Stöffler, D., Knöll, H. D., Marvin, U. B., Simonds, C. H., & Warren, P. H. (1980). Recommended classification and nomenclature of lunar highland rocks—a committee report. In *Lunar highlands crust* (pp. 51–70)
- Taylor, L. A., Patchen, A., Taylor, D.-H. S., Chambers, J. G., & McKay, D. S. (1996). X-ray digital imaging petrography of lunar mare soils: modal analyses of minerals and glasses. *Icarus*, *124*, 500–512. <https://doi.org/10.1006/icar.1996.0226>
- Taylor, L. A., Pieters, C., Keller, L. P., Morris, R. V., McKay, D. S., Patchen, A., & Wentworth, S. (2001). The effects of space weathering on Apollo 17 mare soils: Petrographic and chemical characterization. *Meteoritics & Planetary Science*, *36*, 285–299. <https://doi.org/10.1111/j.1945-5100.2001.tb01871.x>
- Taylor, S. R. (1982). *Planetary science: A lunar perspective*. Lunar and Planetary Institute.
- Thaisen, K. G., Head, J. W., Taylor, L. A., Kramer, G. Y., Isaacson, P., Nettles, J., et al. (2011). Geology of the Moscoviense basin. *Journal of Geophysical Research*, *116*(E6). <https://doi.org/10.1029/2010je003732>
- Tompkins, S., & Pieters, C. M. (1999). Mineralogy of the lunar crust: Results from Clementine. *Meteoritics & Planetary Science*, *34*(1), 25–41. <https://doi.org/10.1111/j.1945-5100.1999.tb01729.x>
- Williams, J.-P., Sefton-Nash, E., & Paige, D. A. (2016). The temperatures of Giordano Bruno crater observed by the diviner lunar radiometer experiment: Application of an effective field of view model for a point-based data set. *Icarus*, *273*, 205–213.
- Yamamoto, S., Nakamura, R., Matsunaga, T., Ogawa, Y., Ishihara, Y., Morota, T., et al. (2010). Possible mantle origin of olivine around lunar impact basins detected by SELENE. *Nature Geosciences*, *3*(8), 533–536. <https://doi.org/10.1038/ngeo897>
- Yamamoto, S., Nakamura, R., Matsunaga, T., Ogawa, Y., Ishihara, Y., Morota, T., et al. (2012). Massive layer of pure anorthosite on the Moon. *Geophysical Research Letters*, *39*, L13201. <https://doi.org/10.1029/2012gl052098>